Cell Systems

Article

Core passive and facultative mTOR-mediated mechanisms coordinate mammalian protein synthesis and decay

Graphical abstract

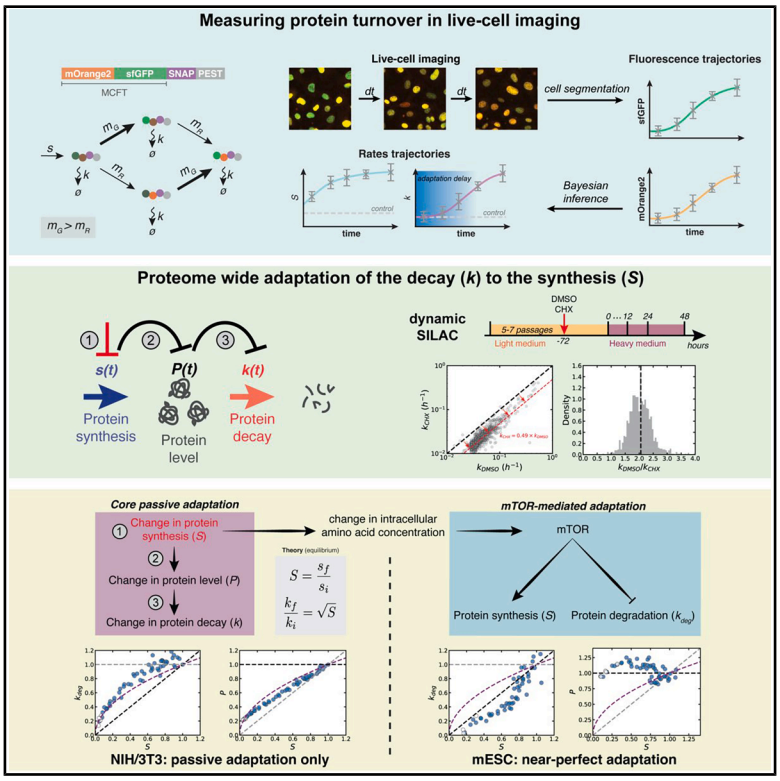

Highlights

- Proteome-wide decay rates adapt to global changes in protein synthesis rate
- A passive mechanism is sufficient to explain this adaptation in most cell types
- An additional mTOR-driven mechanism allows for near-perfect adaptation in naive ES cells
- Divergent adaptation of degradation and dilution rates leads to proteome imbalance

Authors

Michael Shoujie Sun, Benjamin Martin, Joanna Dembska, Ekaterina Lyublinskaya, Cédric Deluz, David M. Suter

Correspondence

david.suter@epfl.ch

In brief

Sun et al. studied how protein decay rates through dilution and active degradation adapt to changes in protein synthesis rates. A passive mechanism is sufficient to explain adaptation in most cell types, except for naive pluripotent stem cells that also leverage the mTOR pathway to achieve near-perfect adaptation.

Sun et al., 2026, Cell Systems *17*, 101456
January 21, 2026
https://doi.org/10.1016/j.cels.2025.101456

CellPress

Cell Systems

CellPress
OPEN ACCESS

Article

Core passive and facultative mTOR-mediated mechanisms coordinate mammalian protein synthesis and decay

Michael Shoujie Sun,[1,2] Benjamin Martin,[1,2] Joanna Dembska,[1] Ekaterina Lyublinskaya,[1] Cédric Deluz,[1] and David M. Suter[1,3,*]

[1]Institute of Bioengineering, School of Life Sciences, Ecole Polytechnique Fédérale de Lausanne (EPFL), 1015 Lausanne, Switzerland
[2]These authors contributed equally
[3]Lead contact
*Correspondence: david.suter@epfl.ch
https://doi.org/10.1016/j.cels.2025.101456

SUMMARY

The maintenance of cellular homeostasis requires tight regulation of proteome concentration and composition. To achieve this, protein production and elimination must be robustly coordinated. However, the mechanistic basis of this coordination remains unclear. Here, we address this question using quantitative live-cell imaging, computational modeling, transcriptomics, and proteomics approaches. We found that protein decay rates systematically adapt to global alterations of protein synthesis rates. This adaptation is driven by a core passive mechanism supplemented by facultative changes in mechanistic/mammalian target of rapamycin (mTOR) signaling. Passive adaptation hinges on changes in the production rate of the machinery governing protein decay and allows for partial maintenance of the cellular proteome. Sustained changes in mTOR signaling provide an additional layer of adaptation unique to naive pluripotent stem cells, allowing for near-perfect maintenance of proteome composition. Our work unravels the mechanisms protecting the integrity of mammalian proteomes upon variations in protein synthesis rates. A record of this paper's transparent peer review process is included in the supplemental information.

INTRODUCTION

Proteins are the central macromolecular components of cellular machinery. The cellular proteome must be constantly turned over to eliminate misfolded or damaged proteins, maintain proteome homeostasis, and to respond to external stimuli. Protein turnover relies on the combined activities of protein synthesis and decay. The rate of protein synthesis is influenced by mRNA concentration and translation rate, whereas protein decay is affected by degradation and dilution through cell growth and division. The ubiquitin-proteasome system (UPS) and autophagy are responsible for the active degradation of proteins and protein complexes. The UPS handles the degradation of most cellular proteins, while autophagy primarily engages in protein degradation during cellular stress.[1] The rates at which proteins are synthesized and degraded can be adjusted to meet cellular needs, regulating the pace of proteome renewal[2,3] for specific cellular function,[4–6] or to achieve a specific growth or division rate.[2,7,8] The contributions of degradation and dilution to protein-specific decay vary widely depending on their degradation rates; for example, short-lived proteins mostly decay through proteasomal degradation, while proteins with half-lives longer than the cell cycle mainly decay by dilution.

The synthesis of new proteins is a highly energy-consuming process that requires a continuous supply of amino acids.[9,10] In multicellular organisms, these resources are subject to large fluctuations and can affect protein turnover rates.[11–14] For example, in humans, food intake can trigger massive increases in protein synthesis rates (up to 100% in the case of muscles[15]). Global protein synthesis rates also change as a function of developmental and differentiation stages,[16,17] in response to pathological stimuli such as viral infection[18] or lipopolysaccharide.[19] The integrated stress response (ISR) and the mechanistic/mammalian target of rapamycin (mTOR) signaling pathways regulate global rates of protein synthesis and decay.[20–23] The ISR can modulate protein synthesis rates in response to cellular stresses, including alterations in protein degradation rates, through the segregation of mRNAs into stress granules to inhibit their translation.[24,25] The mTOR pathway stimulates protein synthesis through increased production of ribosomal proteins and by directly enhancing translation rates.[26] Its role in regulating protein decay is more controversial. While mTOR inhibition was shown to increase protein degradation rates acutely (within 1 h),[27,28] the opposite effect was reported by another study focusing on longer timescales.[29]

Protein synthesis and decay rates need to be tightly coordinated to maintain proteome concentration and composition within a narrow range, thereby ensuring the maintenance of cellular functions.[30] While rates of protein synthesis and decay were shown to be positively correlated in cultured cells,[31] the

mechanisms underlying this coordination are unknown. Here, we show that changes in protein synthesis rates direct the adaptation of protein decay rates through a core passive and a facultative, mTOR-driven active mechanism, and we reveal their implications for the control of proteome concentration and stoichiometry.

RESULTS

Protein decay rates adapt to changes in protein synthesis rates

To monitor protein synthesis and degradation rates in live cells, we used the mammalian cell-optimized fluorescent timer (MCFT),[31] a translational fusion between the fast-maturing sfGFP and the slow-maturing mOrange2 fluorescent proteins (Figure 1A). Because of these differences in maturation rates, the relative changes in green (sfGFP) and red (mOrange2) fluorescence contain information about changes in synthesis and degradation rates[31–33] (supplemental text). We fused the MCFT to a SNAP-tag, which allows for the orthogonal measurement of degradation rates upon pulse labeling with a SNAP-tag dye.[31,34,35] We additionally fused a PEST element to the C terminus, resulting in a high degradation rate (k_{deg}) (Figure S1A) of the fusion protein (short-lived timer-SNAP or SLT). To infer changes in MCFT turnover from fluorescence trajectories, we used a mathematical model (STAR Methods; supplemental text) to compute the protein synthesis rate (S) and distinguish protein decay by active degradation (k_{deg}) from decay through dilution occurring upon cell division (k_{dil}) (Figure S1B). From this model, an analytical relationship between the sfGFP to mOrange2 fluorescence ratio (called G/R hereafter) and the decay rate ($k = k_{dil} + k_{deg}$) of the MCFT can be derived at steady state.

We then asked how the protein decay rate k adapts to changes in global protein synthesis rates S. Note that S itself depends on the availability of the translation machinery, translation efficiency, and the pool of available mRNAs. To allow for global, tunable, fast, and reversible inhibition of global protein synthesis at the level of translation, we decided to use cycloheximide (CHX),[36,37] which blocks the elongation of polypeptide chains by the ribosome. We treated SLT-expressing NIH/3T3 fibroblasts with 56 different concentrations of CHX, ranging from 0.002 to 0.5 μg/mL for 48 h (Figure 1B; Table S1) to fine-tune global translational activity. Crucially, we focused our interpretation on a CHX concentration range at which cells keep proliferating exponentially (up to 0.2 μg/mL; Figure S1C; STAR Methods) to avoid biases caused by altered cellular health. We then performed SNAP pulse-chase labeling followed by live-cell imaging for 12 h while maintaining the respective CHX concentrations (Figure 1C). We used sfGFP and mOrange2 fluorescence intensities to infer changes in S and k (STAR Methods) and used the integrated sfGFP intensity to compute the total MCFT protein amount P. We also measured k_{deg} directly by quantifying the SNAP-SiR647 signal decay (Figure S1D) and measured protein dilution rates (k_{dil}) by quantifying changes in cell numbers (Figure S1E). We used the SNAP-SiR647 pulse-chase experiment to quantitatively calibrate the MCFT (Figure S1F). As expected, S decreased with increasing CHX concentrations (Figure S1G). k_{deg}, k_{dil}, and P decreased with increasing CHX concentrations (Figures S1H–S1J), indicating that the protein degradation and cell-cycle machineries are sensitive to changes in S. Results obtained using SNAP pulse-chase labeling and treatment with different concentrations (Figure S1D) yielded similar results. These results indicate that k adapts partially to changes in S caused by CHX treatment.

We then asked whether the decreased production of protein degradation and dilution machineries, caused by a decrease in S, would be sufficient to explain the partial adaptation of k to S in NIH/3T3 cells. Briefly, we modeled three interdependent sets of proteins: the degradation machinery (DeM), the dilution machinery (DiM), and a protein of interest (POI) (Figure 1D). The degradation and dilution machineries are required for their own decay and the decay of the POI. The model assumes that translation inhibition by CHX scales down S of the DeM, DiM, and the POI by the same factor (Figure 1D). As CHX reduces DeM and DiM synthesis, their protein level decreases, subsequently reducing their decay rate. After reaching equilibrium, the protein level of DeM and DiM and thus the POI decay rate scale as the square root of S, leading to the same scaling for the POI (Figure 1D; supplemental text). We used our SLT data to ask how well our model explains changes in the activity of the degradation and dilution machineries. The passive adaptation model recapitulated the relationships of S with k, k_{deg}, and k_{dil} (Figures 1E–1G), even though k_{deg} stayed slightly more stable than expected upon moderate changes in S (Figures 1F and 1H). This suggests that spare degradation resources allow for k_{deg} to be maintained upon a modest decrease in S. In addition, k_{dil} adapted more than expected at very low S (<0.3), which might be explained by altered cell viability (as assessed by loss of exponential proliferation) in this regime. We also found that changes in P upon changes in S could be approximated by the passive adaptation model (Figure 1I).

To confirm the generality of our findings, we next used other approaches to decrease S. Results obtained with a concentration gradient of another translation inhibitor (anisomycin)[37] (Figures S1K–S1M; Table S2) or of the mTOR inhibitor INK128 (Figures S1N–S1P; Table S3) also followed the passive adaptation model. We also performed an experiment in which we titrated down the concentration of four amino acids (STAR Methods) to decrease translation efficiency. Even though changes in S did not follow changes in amino acid concentration as expected, mostly likely caused by the mobilization of intracellular amino acid pools, the adaptation profile was also similar (Figures S1Q–S1S; Table S4). Finally, we confirmed the passive adaptation model as the most likely scenario for the CHX gradient by log-likelihood computation and bootstrapping for model selection (STAR Methods; Figures S1T and S1U).

We next asked whether changes in k_{deg} and k_{dil}, upon a decrease in S, are interdependent. Since the proteasome is a long-lived machinery,[38–41] we reasoned that in dividing cells, its concentration might be more dependent on k_{dil} than k_{deg}. To test this hypothesis, we took advantage of the global gene expression and cell proliferation regulation by the MYC transcription factor[42] and the availability of a specific MYC inhibitor 10058-F4[43] (MYCi). Since MYC enhances global transcriptional and translational activity and directly activates cell-cycle regulators to stimulate cell proliferation,[42] we reasoned that MYCi would decrease both S and k_{dil} independently. We treated NIH/3T3 cells for 48 h with 56 doses of MYCi, ranging from 0.26 to 64 μM (Figure S1V;

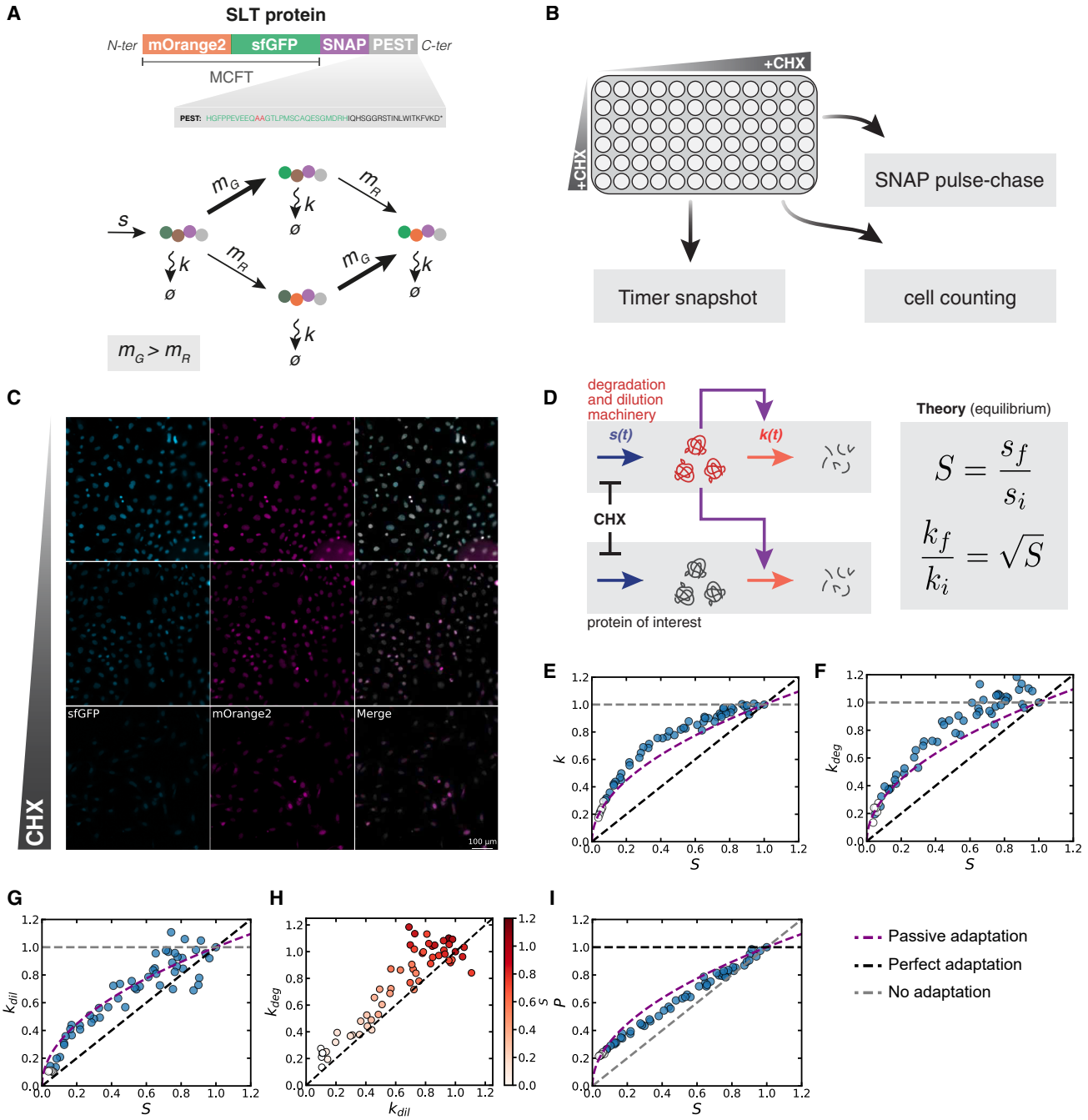

Figure 1. Relationships between *S*, *P*, k_{deg}, and k_{dil} upon CHX treatment follow a passive adaptation model

(A) Scheme of the SLT construct. MCFT, mammalian cell-optimized fluorescent timer.

(B) Experimental design to determine changes in *S*, k_{deg}, k_{dil}, and *P* after treatment with different CHX concentrations.

(C) Representative images of green (cyan) and red (magenta) fluorescence snapshots of ca 30–80 NIH/3T3 cells treated with different CHX concentrations (from top to bottom: 0.008, 0.1125, and 0.5 µg/mL) for 48 h.

(D) Chemical scheme of the passive adaptation model and predicted relationship of *k* and *S* at equilibrium.

(E–G) Fold change in *k* (E), k_{deg} (F), and k_{dil} (G) vs. fold change in *S*.

(H) Fold change in k_{deg} vs. fold change in k_{dil}. Color bar: fold change in *S*. x = y diagonal black dashed line: equal fold change in degradation and dilution rates.

(I) Fold change in *P* vs. fold change in *S*. White dots: data points for which exponential division was lost. Black dashed lines: prediction for perfect adaptation; gray dashed lines: prediction for no adaptation. Purple dashed curved lines: prediction for passive adaptation. The values shown for *S*, *P*, *k*, k_{deg}, and k_{dil} are normalized on the respective values for control conditions and are displayed as arbitrary units, using a linear scale on both axes.

Table S5). As expected, we observed a MYCi dose-dependent decrease in *S* (Figures S1W and S1X) and a strong, close-to-perfect adaptation of k_{dil} to changes in *S* (Figures S1Y and S1Z). In contrast, k_{deg} stayed constant until *S* went below 50% of its value in control conditions (Figures S1AA–S1AC). We also performed a luminescence-based proteasome activity assay (STAR Methods) upon MYCi treatment and found proteasome activity changes to be in line with changes in k_{deg} that we observed by SLT imaging (Figure S1AD). This suggests that a strong decrease in k_{dil} may abolish changes in k_{deg} in response to a decrease in *S* and thereby that k_{deg} is dependent on k_{dil}.

A passive adaptation model explains changes in *P* and *k* for other proteins and cell types

To test the generality of the passive adaptation model, we generated NIH/3T3 cell lines constitutively expressing the MCFT-SNAP with a mutated, non-functional PEST (long-lived timer or LLT) or without PEST and fused to the NANOG, ESRRB, or SOX2 proteins. This resulted in MCFT-labeled proteins characterized by different protein-specific k_{deg} (psk_{deg}) at steady state (Figure S2A) and thus distinct contributions of k_{deg} and k_{dil} to *k* (Figure S2B). Given that the LLT has a very low psk_{deg} (Figure S2A), CHX treatment was extended to 6 days to ensure reaching a steady state. The passive adaptation model recapitulated well the changes in *k* upon CHX treatment for all tested proteins (Figures 2A–2D). To quantify changes of total protein levels, we treated cells with different CHX concentrations for 6 days, labeled all intracellular proteins using N-hydroxysuccinimidyl (NHS) ester that reacts with free amino groups,[30] and quantified changes in the nuclear NHS-ester signal (Figures 2E and S2C). The passive adaptation model explained well the changes in total nuclear protein content at moderate changes in *S*. When reaching very low S levels, changes in total protein levels started to deviate from the passive adaptation model. This can be explained by the long median half-life of proteins in NIH/3T3 cells (16.7 ± 6.2 [median ± SD] h, from Schwanhäusser et al.[44]; supplemental text), which implies a dominant impact of k_{dil} over k_{deg}.

We then asked if passive adaptation could also explain the adaptation of *k* to *S* in other mammalian cell types. We generated a knockin human embryonic stem cell line (hESC) in which the SLT was integrated into the CLYBL locus[45] (Figures S2D–S2F; STAR Methods). Upon treatment with different doses of CHX (Figure 2F), k_{deg} followed the passive adaptation model (Figure 2G), while k_{dil} adapted slightly more efficiently (Figures 2H and 2I). Changes in *P* were well approximated by the passive adaptation model (Figure 2J). We obtained similar results using mTOR inhibition (Figures S2G–S2I).

We then asked how protein decay adapts to changes in protein synthesis rates in differentiated, non-dividing cells. To do so, we differentiated SLT-expressing hESCs into astrocytes[46] (Figures S2J–S2M; STAR Methods). Most cells were negative for the proliferation marker Ki67, indicating their post-mitotic state (Figures S2J–S2M). We then treated SLT-expressing astrocyte-enriched cultures with different concentrations of CHX (Figures S2N and S2O), and we found that *k* and *P* followed the passive adaptation model (Figures 2K and 2L). We also generated induced neurons from hESCs carrying inducible expression of NGN1 and NGN2, allowing rapid generation of post-mitotic neurons (Figures S2P–S2R; STAR Methods). We performed a CHX plate experiment followed by NHS-ester staining to quantify total protein content, and we used L-homopropargylglycine (HPG) labeling to quantify changes in *S* (STAR Methods). We found that total protein content in human neurons also followed the passive adaptation model (Figures 2M and S2S–S2U). Taken together, these data suggest that passive adaptation of the decay rate *k* to the synthesis rate *S* also occurs in the absence of cell division in differentiated post-mitotic cells.

k adapts to *S* within 10 h

We then developed a superstatistical Bayesian approach[47–49] to infer time variations of *S* and *k* from MCFT traces (Figure S3A; STAR Methods; supplemental text). To validate our inference method, we generated synthetic sfGFP and mOrange2 fluorescence trajectories (Figures S3B and S3C) imposing defined variations of *S* and *k*. Our inference robustly recovered ground-truth time variations of *S* and *k* from the fluorescence trajectories (Figures S3D and S3E).

We next used a cell line in which MCFT expression is controlled by a doxycycline (Dox)-inducible promoter in NIH/3T3 cells,[31] allowing the alteration of the synthesis rate of the MCFT only, without expected changes in its psk_{deg}. We used 28 different step changes in Dox concentrations (Figure 3A) and quantified sfGFP and mOrange2 fluorescence over time (Figure S3F). In all cases, we correctly inferred expected changes in *S* and a mostly unaltered *k* (Figure 3A). Furthermore, data retrodiction (STAR Methods; supplemental text) confirmed that our inference accurately reproduces the input data (Figure S3G). We conclude that our inference scheme allows for robust discrimination between changes in *S* and *k* from time traces of the MCFT.

We then aimed at quantifying the timescales characterizing the adaptation of *k* to alterations in *S*. To do so, we performed time-lapse imaging of the MCFT in NIH/3T3 constitutively expressing the SLT before, during treatment with 0.1 μg/mL of CHX and after CHX release (Figure 3B; Videos S1 and S2). We then used our inference algorithm to determine changes in *S* and *k* from SLT fluorescence time traces. Upon CHX treatment, *S* sharply decreased (Figure 3C), while *k* progressively decreased until reaching a lower plateau (Figure 3D). To quantify the adaptation time delay of *k* to *S*, we used a metric (θ) that we recently developed, which allows for quantifying the imbalance between protein influx (governed by *S*) and outflux (governed by *k*).[50] Briefly, the imbalance reads $\theta = Pk/S$, such that at equilibrium, $\theta = 1$ or $\theta > 1$ or < 1 indicates an excess of protein outflux or influx, respectively.[50] θ reached its steady-state value around 10 h after CHX addition (Figure 3E). Upon CHX release, we observed similar dynamics and delay in the adaptation of *k* to *S* and in θ (Figures 3F–3H). We performed the same CHX pulse and release experiments in hESCs (Videos S3 and S4), which resulted in a similar delay in the adaptation of *k* to *S* (Figures 3I–3N). We then also performed SNAP-tag pulse labeling at different time points after CHX release on the SLT in NIH/3T3, which yielded similar results (Figures S3H–S3K). Finally, we also performed MYCi pulse and release experiments in NIH/3T3, and we found that *S* and *k* reached a steady state within a similar time frame (Figures S3L–S3Q).

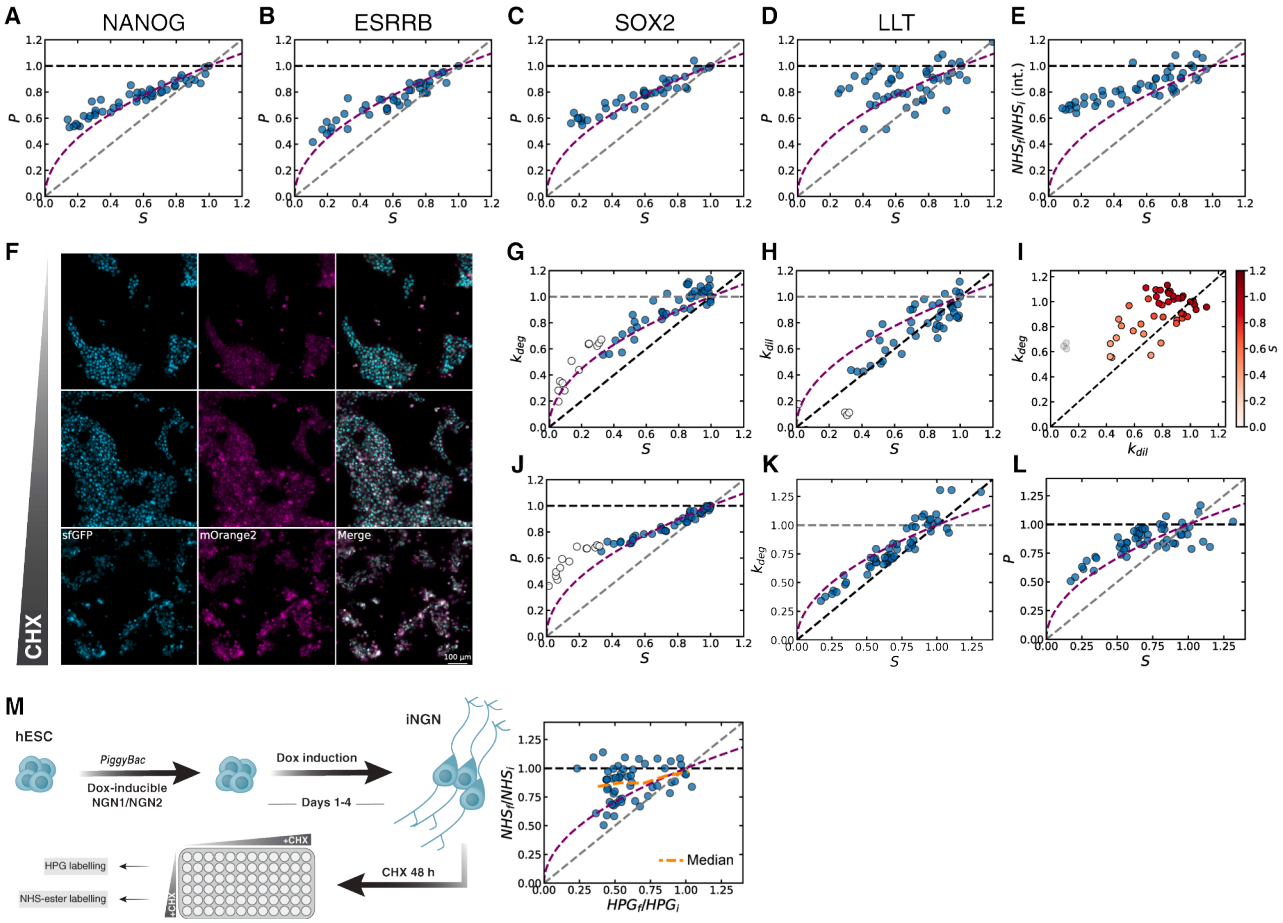

Figure 2. Passive adaptation of *k* and *P* to *S* for other proteins and for SLT in hESCs and hESC-derived astrocytes

(A–D) Fold change of *P* with respect to *S* for NANOG (A), ESRRB (B), SOX2 (C), and the LLT (D).

(E) Fold change in total nuclear protein levels with respect to *S*, measured with NHS-ester.

(F) Representative images of green (cyan) and red (magenta) fluorescence snapshots of ca 100–300 hESC SLT cells treated with different CHX concentrations (from top to bottom: 0.008, 0.1125, and 0.5 μg/mL) for 48 h.

(G and H) Fold change in k_{deg} (G) and k_{dil} (H) vs. fold change in *S* in hESCs.

(I) Fold change in k_{deg} with respect to the change in k_{dil} in hESCs treated with CHX. Color bar: fold change in *S* in each condition.

(J) Fold change in *P* vs. *S* for CHX treatment in hESCs.

(K) Fold change in k_{deg} vs. fold change in *S* for CHX treatment in human astrocyte-enriched culture.

(L) Fold change in *P* vs. *S* for CHX treatment in human astrocyte-enriched culture.

(M) Fold change in total nuclear protein levels with respect to fold change in global *S* in iNGNs, measured, respectively, with NHS-ester and HPG labeling.

(A–E, G, H, and J–M) Black dashed lines: prediction for perfect adaptation; gray dashed lines: prediction for no adaptation. Purple dashed curved lines: prediction for passive adaptation. White dots: data points for which exponential division was lost. The values shown for *S*, *P*, k_{deg}, and k_{dil} are normalized on the respective values for control conditions and are displayed as arbitrary units, using a linear scale on both axes.

Naive mESCs display a distinct, biphasic adaptation mode

Next, we aimed to characterize the adaptation of *k* and *P* to *S* in naive mouse embryonic stem cells (mESCs). mESCs display a modified cell cycle with an altered G1-S checkpoint and an inactive Rb protein.[51] Rb allows coordination of cell growth—itself dependent on protein content accumulation—and cell division.[52] We thus reasoned that in mESCs, k_{dil} may react differently to changes in *S*, as compared with NIH/3T3 and hESCs. We generated a mESC line in which the SLT is knocked into the ROSA26 locus[53] (Figures S4A–S4C; STAR Methods) and quantified the response of *k* and *P* to changes in *S* (Figures 4A–4E). In contrast to NIH/3T3 and hESCs, k_{deg} over-adapted to changes in *S* (Figure 4B), and k_{dil} remained high until *S* dropped below circa 60% of its maximal value (Figures 4C and 4D). Both the SLT and NHS-ester-stained nuclear proteome remained virtually unchanged upon a decrease in *S*, underscoring the close-to-perfect adaptation of *k* to *S* (Figures 4E, 4F, and S4D). Interestingly, an mTOR concentration gradient experiment resulted in a less efficient adaptation of *k* and *P* to *S* (Figures S4E–S4G), suggesting that the mTOR pathway may be involved in mESC adaptation.

We next asked whether mESC pluripotency is impacted by changes in protein turnover. We performed immunofluorescence

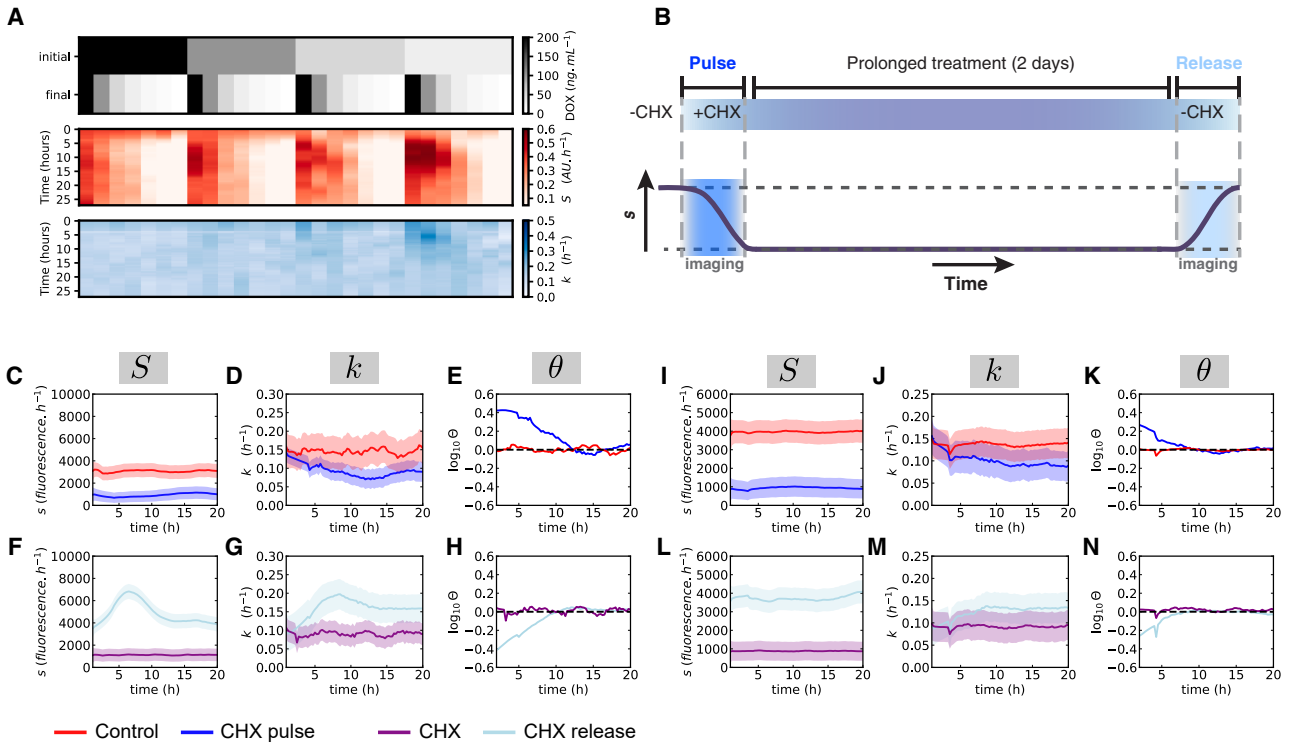

Figure 3. Passive adaptation occurs with a timescale of 5–15 h

(A) Upper: Dox concentration changes between the initial and final concentrations used just before imaging. Heatmaps: temporal variations of *S* (red) and *k* (blue) inferred from SLT trajectories.

(B) Experimental design of CHX pulse and release experiments.

(C–N) Time-lapse imaging for NIH/3T3 (C–H) and hESCs (I–N). *S* (C and I) and *k* (D and J) trajectories inferred from MCFT measurements during CHX pulse. Red: control conditions. Dark blue: CHX pulse. Purple: continuous CHX treatment. Light blue: CHX release. (E and K) Time variation of the imbalance for the CHX pulse. *S* (F and L) and *k* (G and M) trajectories inferred from MCFT measurements during CHX release. (H and N) Time variations of the imbalance for CHX release. (C–G and I–M) Plain lines: average of the posterior distribution; shaded regions: SD of the posterior distribution. All values plotted are displayed using a linear scale on both axes.

for markers of pluripotency (NANOG, SOX2, OCT4) after culturing mESCs in the absence or presence of CHX at four different concentrations (0.025, 0.05, 0.1, or 0.2 μg/mL) for 72 h. Expression of pluripotency markers was preserved at all CHX concentrations (Figure S4H), suggesting that pluripotency maintenance was not altered by CHX treatment.

We then performed time-lapse imaging to monitor changes in *k* upon a 0.1 μg/mL CHX pulse (Video S5) and release (Video S6). *S* initially dropped upon CHX addition but rapidly increased thereafter before dropping again to reach a slightly higher value than immediately after CHX addition (Figure 4G). *k* was decreased immediately at the beginning of imaging and stabilized after about 10 h (Figures 4H and 4I). This suggests that an active, fast-acting mechanism allows for CHX inhibition to be partially counteracted and for protein degradation to be rapidly shut down upon decrease of *S*. Upon CHX release, we observed a rapid increase in *S* that then dropped again, before increasing to levels of control conditions (Figure 4J), while *k* showed a rapid initial increase and reached steady state toward the end of the imaging period (∼20 h) (Figures 4K and 4L). Therefore, mESCs adopt a biphasic adaptation mode in which k_{deg} and *S* respond to CHX within a few hours, but full adaptation occurs in a slower second phase.

Physiological variability in protein turnover recapitulates cell-type-specific adaptation

To ensure that the adaptation we uncovered is not caused by unspecific effects of translation inhibitors and that it reflects physiological changes of *k* in response to fluctuations in *S*, we took advantage of the natural fluctuations of *S* in unperturbed conditions[31] and determined the relationship between *S*, *k*, and *P* at the single-cell level. We used time-lapse imaging data acquired in the absence of perturbation in (1) 5 NIH/3T3 cell lines expressing the SLT, LLT, and the MCFT fused to NANOG, ESRRB, and SOX2, respectively, and in (2) 40 mESC lines in which the MCFT is internally fused to 40 different endogenously expressed proteins.[31] We have previously shown that the majority of these 40 proteins exhibit only minor fluctuations in *S*, *k*, and protein concentration [*P*] over the cell cycle in single cells.[31] This quasi-steady state allows us to compute *k* for single cells as before for population averages (STAR Methods). Similarly, we computed $S_{conc.}$ and [*P*] for single cells. Note that $S_{conc.}$ is a per-cell protein synthesis rate in concentration per hour unit (STAR Methods). Since $S_{conc.}$ does not correlate with nucleus size (Figures S5A and S5B), it can be considered a proxy of single-cell protein synthesis rate, *S* being proportional to its population average. To determine the relationship between

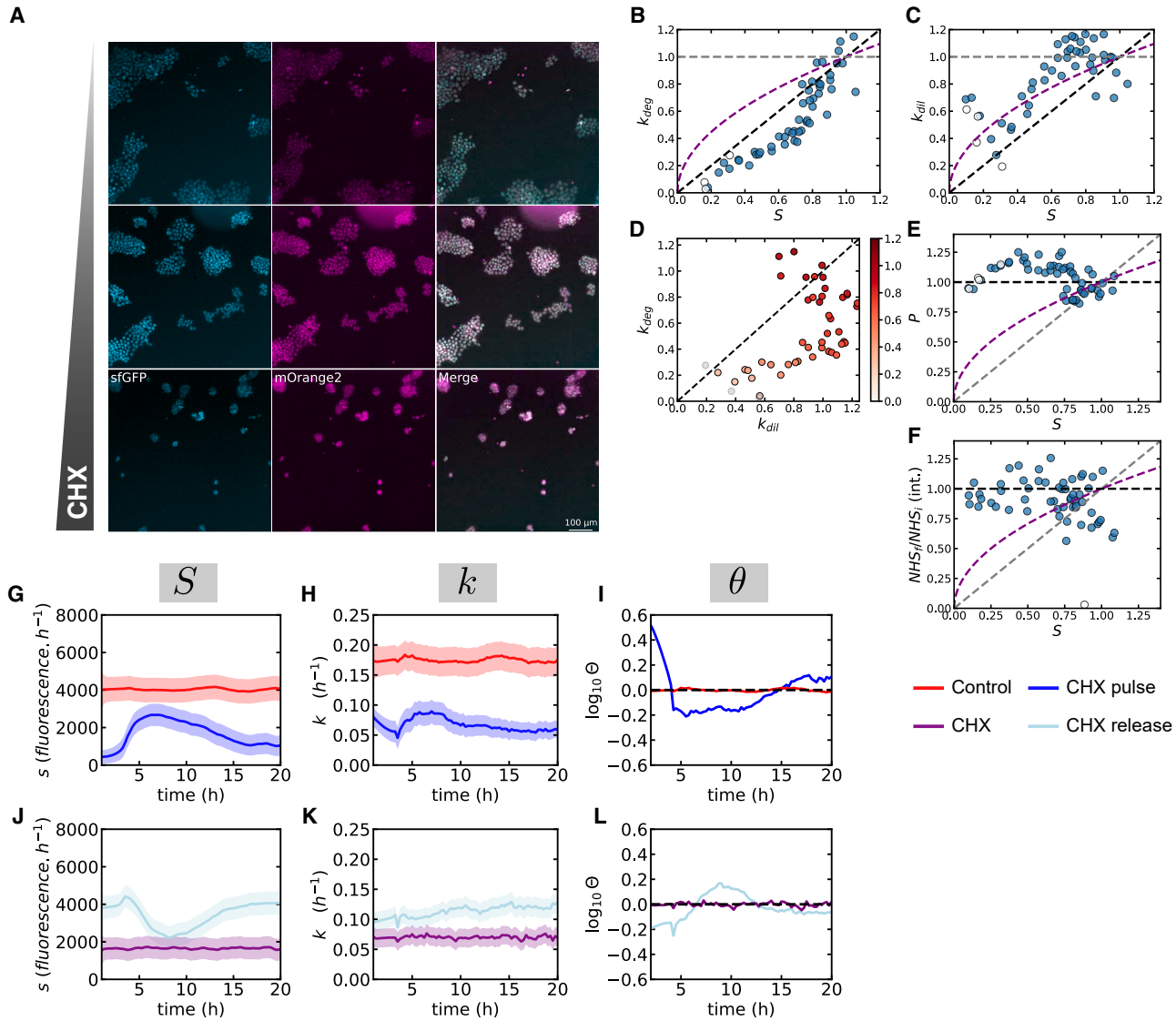

Figure 4. mESC adaptation is inconsistent with a purely passive mechanism

(A) Representative images of green (cyan) and red (magenta) fluorescence snapshots of ca 100–500 mESC SLT cells treated with different CHX concentrations (from top to bottom: 0.008, 0.1125, and 0.5 μg/mL) for 48 h.

(B and C) Changes in k_{deg} (B) and k_{dil} (C) vs. S for CHX treatment in mESCs.

(D) Changes in k_{deg} vs. k_{dil} in mESCs treated with CHX. Color bar: fold change in S.

(E) Changes in P vs. S for the SLT.

(F) Fold change in total nuclear P vs. S, measured with NHS-ester staining intensity (int.).

(B, C, E, and F) Black dashed lines: prediction for perfect adaptation; gray dashed lines: prediction for no adaptation. Purple dashed curved lines: prediction for passive adaptation. (B–F) The values shown for S, P, k_{deg}, and k_{dil} are normalized to the respective values for control conditions.

(G and H) S (G) and k (H) trajectories inferred from MCFT measurements during CHX pulse.

(I) Time variation of the imbalance for CHX pulse.

(J and K) S (J) and k (K) trajectories inferred from MCFT measurement during CHX release.

(L) Time variation of the imbalance for CHX release. Red: control conditions. Dark blue: CHX pulse. Purple: continuous CHX treatment. Light blue: CHX release. For (G), (H), (J), and (K), the average (plain line) and the SD (shaded region) of the posterior distribution are represented for each time point. The values shown for k_{deg}, k_{dil}, and NHS_f/NHS_i (int.) are normalized on the respective values for control conditions and are displayed as arbitrary units. All plots are displayed using a linear scale on both axes.

the cell cycle and protein turnover, we looked at the quantitative relationship between G/R ratios and cell-cyclee length, and we found these parameters to be uncorrelated (Figures S5C and S5D). Note also that CHX treatment in NIH/3T3 and mESCs did not impact the distribution of cells in different cell-cycle phases (Figures S5E and S5F). Taken together, this suggests that variability in cell-cycle duration does not impact protein turnover and that forced changes in S impact all cell-cycle

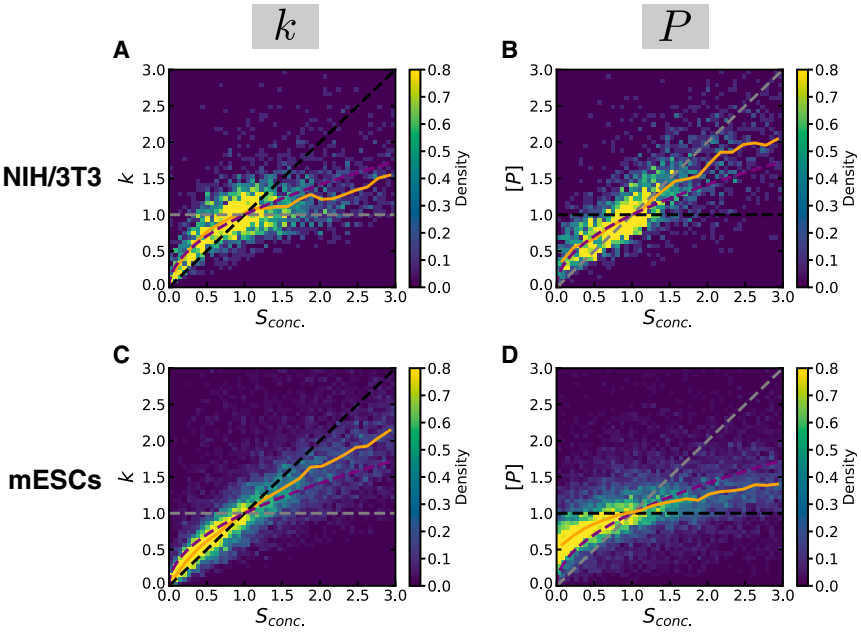

Figure 5. Adaptation of *k* and [*P*] to S_{conc} in unperturbed conditions

(A and B) *k* (A) and [*P*] (B) vs. S_{conc} in NIH/3T3 cells. (C and D) *k* (C) and [*P*] vs. S_{conc} (D) in mESCs. 2D histograms for aggregated and normalized data for 5 (NIH/3T3) or 40 (mESCs) cell lines are shown. n > 4,000 (NIH/3T3) or >10,000 (mESC) cells. Black dashed lines: prediction for perfect adaptation; gray dashed lines: prediction for no adaptation. Purple dashed curved lines: prediction for passive adaptation. Orange plain line: binned median of the aggregated data. The values shown for S_{conc}, [*P*], and *k* are normalized on their mean values and are displayed as arbitrary units, using a linear scale on both axes.

phases equally. We then normalized the data from all proteins to their median value for S_{conc}, *k*, and [*P*], and aggregated all data points. In NIH/3T3 cells, the correlations of *k* and [*P*] with S_{conc} followed the passive adaptation model (Figures 5A and 5B). By contrast, in mESCs, the correlation between S_{conc} vs. *k* and [*P*] was closer to perfect adaptation (Figures 5C and 5D). Altogether, our data demonstrate that cell-type-specific adaptation modes of *k* to *S* are operating upon physiological fluctuations of *S*.

Sustained changes in mTOR signaling drive robust adaptation in mESCs

Changes in global translation rates, including those elicited by CHX treatment, can modulate mTOR activity by altering the intracellular concentration of free amino acids.[36,37,54–58] Since mTOR activity regulates both *S* and *k*, we asked whether changes in mTOR activity contribute to the adaptation of *k* to *S*. We first quantified mTOR activity by measuring phosphorylation of the mTOR target p70S6K after 1, 2, 5, and 48 h of 0.1 μg/mL CHX treatment by ELISA assay in NIH/3T3 cells and mESCs. In line with previous work showing that CHX can activate mTOR signaling,[27,59–63] mTOR activity acutely increased and peaked after 2 h in both cell types before slowly decreasing, albeit to a lesser extent in mESCs as compared with NIH/3T3 cells (Figure 6A). We next asked whether changes in ribosomal protein gene expression in mESCs, which are targets of mTORC1,[64] could explain the rebound in *S* and its elevated levels after circa 20 h of CHX, compared with the earliest time points (Figure 4G). We performed RNA sequencing (RNA-seq) at different time points (0, 1, 2, 5, 48 h) after CHX pulse. Within the first hours of CHX treatment, ribosomal protein genes were markedly upregulated in mESCs but more modestly in NIH/3T3 cells, and after 48 h, they decreased below their initial levels in NIH/3T3 but not mESCs (Figures S6A–S6C). Other genes involved in protein turnover (proteasomal and mitochondrial genes) followed the same dynamics but with a smaller amplitude. Taken together, this suggests that mESCs exhibit a stronger and more sustained adaptation of mTOR signaling and expression of ribosomal protein genes than NIH/3T3 cells.

We next performed CHX pulse time-lapse imaging in mESCs and NIH/3T3 with and without the mTOR inhibitor INK128 or the ISR inhibitor ISRIB. Cells were pre-treated with INK128 or ISRIB for 1 h prior to imaging. In both mESCs and NIH/3T3 cells, 200 nM ISRIB led to slightly increased *S*, but the response of *k* was similar to the one of untreated cells, indicating that the ISR is not required for the adaptation of *k* to *S* (Figures S6D–S6G). Since a full inhibition of the mTOR pathway causes mESCs to stop proliferating and enter diapause,[65,66] we used a low INK128 dose (25 nM) that allowed mESCs to maintain their proliferation rate (Figure S6H). In NIH/3T3, INK128 alone markedly decreased *S*, and *k* adapted to changes in *S* following the passive adaptation model (Figures 6B–6D and S6I). When combined with CHX, INK128 had almost no impact on the dynamic changes in *S* and *k* for up to 18 h (Figures 6B–6D). This suggests that in NIH/3T3 cells, mTOR activity is important to sustain *S* but is not involved in the adaptation of *k* to changes in *S*. In mESCs, 25 nM of INK128 had virtually no impact on *S* in the absence of CHX (Figures 6E–6G). However, the rapid initial boost in *S* and decrease in k_{deg} caused by CHX were impaired by mTOR inhibition. In the longer term (>15 h), mTOR inhibition in the presence of CHX resulted in strongly decreased S levels, compared with CHX alone, and under-adaptation of *k* to changes in *S* (Figures 6E–6G and S6J). Since INK128 did not impact k_{dil} in mESCs (Figure S6H), this suggests that mTOR activity directly contributes to the adaptation of k_{deg} to *S* in mESCs.

We then further investigated the role of mitogen-activated protein kinase (MAPK), which has also been involved in controlling protein synthesis,[67] in the adaptation of NIH/3T3 cells. We combined the CHX concentration gradient with the SP600125 JUNK inhibitor of the MAPK pathway. Note that we did not test this inhibitor in mESCs since our 2i/LIF culture medium contains the PD98059 MAPK inhibitor. In contrast to ISRIB, which, as expected, slightly increased *S* in cells treated with CHX (Figures S6K–S6M), SP600125 treatment decreased *S*. However, the relationship between *S* and *k* still followed the passive

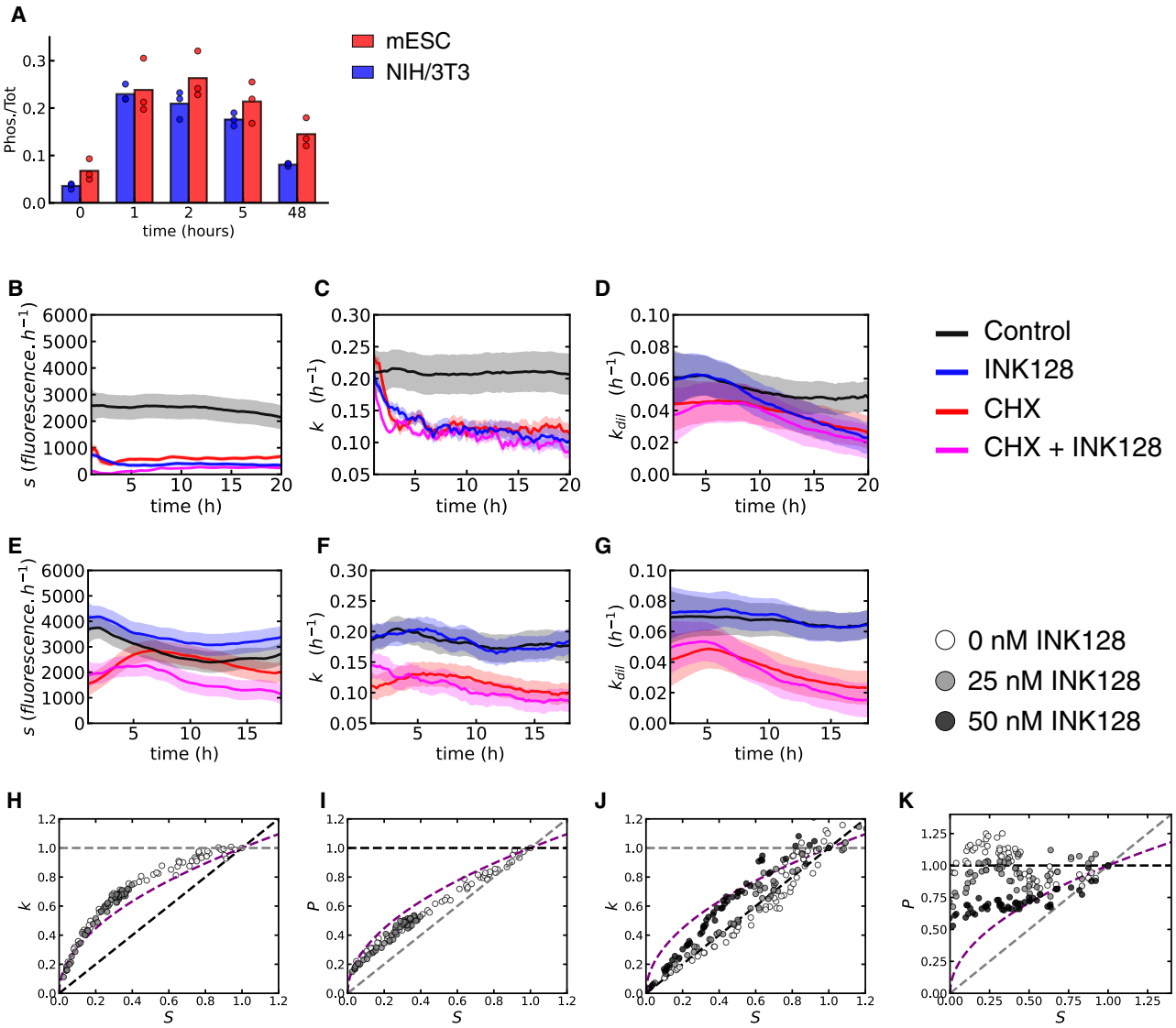

Figure 6. mTOR-dependence of the mESC response to protein synthesis inhibition

(A) Phosphorylation kinetics of p70S6K measured by ELISA after CHX treatment (0.1 μg/mL) in mESC and NIH/3T3.

(B–D) *S* (B), *k* (C), and k_{dil} (D) trajectories inferred from MCFT (*S* and *k*) and cell number (k_{dil}) measurements during CHX pulse for NIH/3T3 cells.

(E–G) *S* (E), *k* (F), and k_{dil} (G) trajectories inferred from MCFT (*S* and *k*) and cell number (k_{dil}) measurements during CHX pulse for mESCs. Black: control conditions. Red: CHX treatment. Blue: 25 nM INK128 treatment. Pink: CHX + 25 nM INK128 treatment. The average (plain line) and the SD (shaded region) of the posterior distribution are represented for each time point.

(H–K) Fold change in *k* (H and J) or *P* (I and K) vs. fold change in *S* for NIH/3T3 cells (H and I) or mESCs (J and K) upon long-term treatment with different CHX concentrations in the presence of 0, 25, or 50 nM of INK128. Black dashed lines: prediction for perfect adaptation. Gray dashed lines: prediction for no adaptation. Purple dashed curved lines: prediction for passive adaptation. $n > 1{,}000$ cells for all experiments. The values shown for *k* and *P* in (H)–(K) are normalized on the respective values for control conditions and are displayed as arbitrary units. All plots use a linear scale on both axes.

adaptation model (Figures S6N–S6P). We then repeated the CHX plate experiment in NIH/3T3, hESCs, and mESCs in the presence of either 25 or 50 nM of INK128. In NIH/3T3, while 50 nM of INK128 resulted in massive cell death, 25 nM INK128 combined with CHX resulted in a synergistic impact on *S*, but *k* and *P* were still aligned with the passive adaptation model (Figures 6H, 6I, and S6I). In hESCs, the combination of INK128 with the CHX gradient was also consistent with the passive adaptation model (Figures S6Q and S6R). By contrast, in mESCs, INK128 weakened the adaptation of *k* to *S* in a dose-dependent manner, closely mimicking passive adaptation at 50 nM until $S = 0.3$, matching regimes below which exponential proliferation becomes less robust (Figures 4B, 4C, 6J, and 6K). This is also in line with our mESC INK128 concentration gradient experiment showing a less efficient adaptation than with CHX (Figures S4E–S4G). Altogether, our results indicate that mESCs complement passive adaptation by a sustained adjustment of mTOR signaling, resulting in robust adaptation of k_{deg} to *S*.

Proteome composition and dynamics upon passive and mTOR-driven adaptation

We next quantified long-term changes in the proteome of mESCs and NIH/3T3 upon CHX treatment. We cultured NIH/3T3 cells and mESCs for 4 and 2 days, respectively, with or without 0.1 μg/mL of CHX. We chose these respective CHX treatment durations to maximize the likelihood of reaching a new steady state for all proteins, based on the respective cell-cycle durations of NIH/3T3 (ca 22h) and mESCs (ca 12h). We then extracted proteins and performed label-free quantification (LFQ) mass spectrometry (STAR Methods). While 10% and 2.8% of proteins were downregulated or upregulated in NIH/3T3 (Figures 7A and 7B), respectively, only 0.6% and 0.1% were downregulated or upregulated in mESCs (Figures 7C and 7D). At this CHX concentration, the immediate impact on S levels was even stronger in mESCs than in NIH/3T3 cells (earliest time points in Figures 3C and 4G), suggesting that mESCs have a superior ability to maintain their protein levels upon perturbation of *S*. Ribosomal proteins were well preserved in both cell types, but proteins involved in mitochondrial or proteasomal functions were slightly downregulated in NIH/3T3 cells but not in mESCs (Figures S7A–S7C), in line with passive adaptation of cellular resources governing protein decay in NIH/3T3.

To determine the proteome-wide adaptation of k to changes in S, we performed dynamic stable isotope labeling by amino acids in cell culture (dSILAC[19,44,68–70]) (Figure S7D; STAR Methods; supplemental text) in the presence or absence of 0.05 μg/mL of CHX during 72 h, for both NIH/3T3 and mESCs. We used a CHX concentration of 0.05 μg/mL to avoid total arrest of cell growth for NIH/3T3 cells cultured in the SILAC DMEM medium, which lacks growth factors (STAR Methods). Cellular proteins were initially labeled using a medium containing light (NIH/3T3) or medium (mESC) arginine and lysine amino acids, which was then exchanged for a medium containing heavy (NIH/3T3) arginine and lysine. Samples were collected 0, 1, 2, 4, 6, 12, and 24 h (plus 48 h for NIH/3T3) after medium exchange. After protein extraction, sample preparation and mass spectrometry data were fitted to compute the decay rate per protein (STAR Methods). The decay rate was determined for 2,050 (DMSO) and 2,629 (CHX) proteins in NIH/3T3 and for 3,102 (DMSO) and 3,380 (CHX) proteins in mESCs. The k we inferred for NIH/3T3 proteins correlated strongly with previous NIH/3T3 dSILAC data[44] (Figure S7E). Upon CHX treatment, virtually all proteins exhibited a decreased k in both NIH/3T3 and mESCs (Figures 7E–7H, S7F, and S7G), confirming the proteome-wide impact of changes in S on k. LFQ analysis of protein levels using the 0-h time point confirmed that also for identical CHX treatment durations, NIH/3T3 displayed larger changes in protein levels than mESCs (Figures S7H and S7I). Note that while our dSILAC approach does not allow us to directly measure changes in S, we assumed that CHX should impact S of all proteins similarly, which is confirmed by the very similar changes in S we observed at given CHX doses for different proteins in NIH/3T3 (Figure S7J).

We next reasoned that a quantitatively different adaptation of k_{dil} vs. k_{deg} in NIH/3T3 and mESCs should result in distinct changes of k and P for proteins with different psk_{deg}. We found that despite the fact that NIH/3T3 and mESCs are proliferating cells and that a large fraction of the proteome detected by mass spectrometry is long-lived, k_{deg} contributed to >50% of k for about 30% of proteins in both NIH/3T3 and mESCs (Figures S7K and S7L). In NIH/3T3, k_{dil} adapted slightly better than k_{deg}, while the opposite was true in mESCs. This implies that in NIH/3T3, k_{deg}-dominated proteins (high psk_{deg}) should experience a weaker adaptation of k. Conversely, in mESCs, the k_{dil}-dominated proteins (low psk_{deg}) should experience a weaker adaptation of k. Changes in k upon CHX treatment as a function of the psk_{deg} calculated from our dSILAC data in control conditions closely matched these predictions (Figures 7I, 7J, S7M, and S7N). In line with these findings, protein levels were preferentially decreased for proteins with high psk_{deg} in NIH/3T3 cells but not in mESCs (Figures 7K and 7L). Therefore, cell-type-specific adaptation modes have distinct, predictable consequences on the regulation of proteome homeostasis upon fluctuating protein synthesis rates.

DISCUSSION

Here, we present a microscopy and computational approach allowing us to uniquely quantify protein synthesis and decay rates from both snapshots and time-lapse imaging data. This enabled us to quantify protein turnover dynamics at an unprecedented temporal resolution. While it was known for a long time that full protein synthesis inhibition by CHX treatment impacts protein degradation,[36,71] we here unraveled the quantitative and causal relationship between protein synthesis and decay rates by using several independent perturbations of protein synthesis. This allowed us to build a quantitative model based on a passive adaptation mechanism, which allows for partial adaptation of protein decay to protein synthesis rates, resulting in imperfect proteome maintenance. An additional mTOR-driven adaptation layer allows naive mouse pluripotent stem cells to further optimize the adaptation of protein degradation rates to protein synthesis rates, leading to near-perfect maintenance of their proteome (Figure 7M).

Our passive adaptation model hinges on structural relationships between protein synthesis and the protein decay machinery. While changes in active protein degradation strongly depend on the protein dilution rate in dividing cells, non-dividing cells such as astrocytes also modify their protein degradation rate in response to fluctuations in protein synthesis rates in a quantitatively similar way. This suggests that the turnover of their DeM is actively regulated, consistent with observations that non-dividing cells exhibit a higher degradation rate for long-lived proteins than dividing cells.[72] Passive adaptation allows only for partial maintenance of overall protein levels, but the roughly comparable adaptation of k_{deg} and k_{dil} in dividing cells mitigates the imbalance between proteins decaying mainly through dilution vs. degradation.

Previous studies have shown that mechanisms of cell size control coordinate synthesis and degradation rates to reach a certain target cell size and that growth rate and cell-cycle length are coordinated.[73,74] Interestingly, a delay of about 10 h was also found to coordinate changes in cell size and protein turnover upon perturbation of cell-cycle progression.[73,74] Liu and colleagues[73] observed an increased k_{deg} upon an increase in cell size. Since they used total protein content to determine cell size, this suggests that this increased k_{deg} might have been directly mediated by changes in P and thus by passive

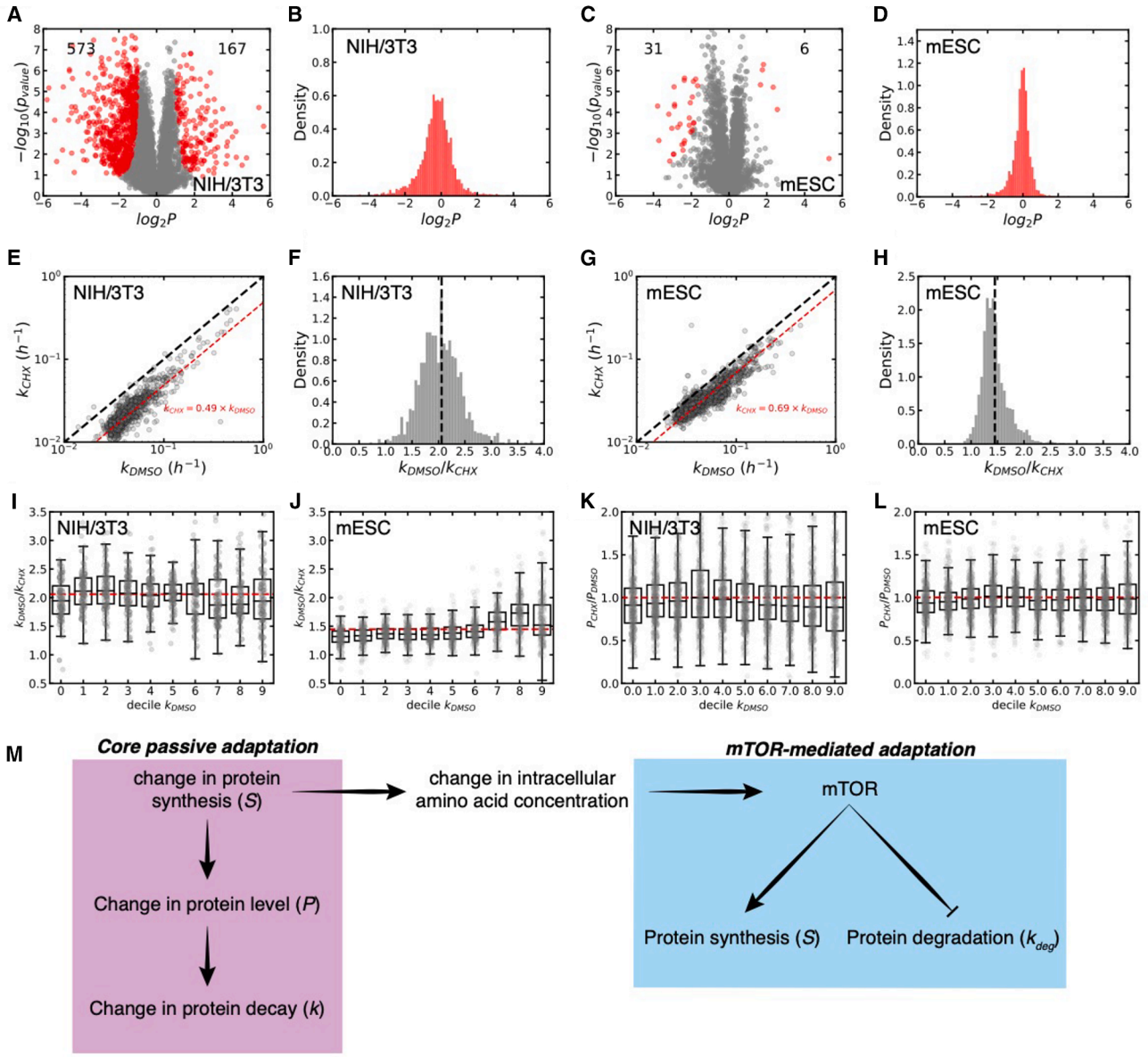

Figure 7. Proteome-wide impact of a prolonged decrease in *S*

(A–D) Label-free proteome quantification for NIH/3T3 cells (A and B) or mESCs (C and D) treated with CHX, leading to the identification of 5,875 and 4,503 proteins, respectively. (A and C) The average of four replicates is plotted for all identified proteins. Red dots: proteins with significant (false discovery rate [FDR] = 0.01) fold change in their levels between CHX and control conditions. Each point is the average over quadruplicates of the protein-specific-level fold change. (B and D) Distribution of protein-level fold changes between CHX and control conditions.

(E and G) Decay rate in (0.05 μg/mL) CHX vs. in DMSO condition for proteins measured in dSILAC (Figure S8; STAR Methods), for NIH/3T3 (E) and mESCs (G). The black dotted line represents $k_{CHX} = k_{DMSO}$. The red dotted line represents the mean fold change in decay rate between CHX and DMSO conditions.

(F and H) Density of the ratio of the decay rates computed in DMSO, k_{DMSO}, and CHX, k_{CHX}, conditions for unique proteins in NIH/3T3 (F) and mESCs (H). Densities (B, D, F, and G) are shown as arbitrary units.

(I and J) Measured decay rate fold change between CHX and control conditions, for NIH/3T3 (I) and mESC (J), binned according to psk_{deg} in DMSO condition.

(K and L) Measured protein-level fold change between CHX and control conditions, for NIH/3T3 (K) and mESC (L), binned according to psk_{deg} in DMSO condition.

(M) Model of core passive and facultative mTOR-mediated coordination of protein synthesis and degradation. All plots are displayed using a linear scale on both axes.

adaptation. In our study, we did not find a correlation between protein turnover and cell size or cell-cycle duration, nor was cell-cycle phase distribution altered by CHX treatment. Therefore, it remains unclear whether the adaptation of *k* and *P* to *S* we describe here explains the relationships between cell size and protein turnover observed in previous studies.

In contrast with other cell types, mESCs robustly decrease k_{deg} and partially rescue translational efficiency upon a decrease

of translational resources through their ability to sustainably increase mTOR signaling. This additional adaptation layer further improves the resilience of the mESC proteome, resulting in near-perfect maintenance of protein levels when their translational capacity is impaired. Interestingly, hESCs, which in our culture conditions are more similar to post-implantation embryo pluripotent stem cells (or primed pluripotent stem cells),[75] did not display mTOR-dependent adaptation. It has also been shown that mESCs and hESCs have a particularly low basal mTOR activity when in the naive state, which increases in the primed state.[76,77] This suggests that naive pluripotent stem cells may have more room for further activation of mTOR signaling to boost protein synthesis and decrease protein degradation when facing limitations in protein synthesis resources. Interestingly, mESCs and the inner cell mass of the pre-implantation blastocyst use a unique strategy for their amino acids supply, based on extracellular protein uptake.[78] This mechanism may explain the robust viability of the pre-implantation embryo even in the absence of exogenous amino acids,[79] which may be complemented by the adaptation mechanisms we describe here to maximize proteome resilience of the early embryo.

Our work has further methodological and biological implications beyond the model systems we used. First, the rapid and universal adaptation of protein decay to changes in protein synthesis rates directly questions the relevance of the CHX pulse approach to determine protein half-lives.[36,80] Second, two views conflict on the predominant roles of species-specific differences in protein synthesis[81] vs. degradation rates[82,83] in regulating the pace of somitogenesis. We argue that the fundamental interconnection between protein synthesis and protein degradation rates makes it extremely challenging to causally address the functional relevance of these rates independently. Third, mTOR inhibition was both reported to decrease[29] and increase[27] protein degradation rates. We found that increased mTOR activity upon a decrease in translational resources contributes to a further decrease in protein degradation rate, in agreement with Zhao et al.[27] However, the modulation of protein synthesis by mTOR signaling indirectly influences protein degradation rates through passive adaptation, in line with decreased protein degradation rates observed during long-term (>16 h) mTOR inhibition.[29]

In summary, our study unravels the pivotal resilience mechanisms that mammalian cells leverage to buffer variations of proteome concentrations when confronted with fluctuations in resources governing protein synthesis rates.

Limitations of the study

To measure proteome-wide adaptation of k in response to alterations in S, we opted for a two-channel SILAC approach, which precludes direct measurements of S. While three-channel SILAC could theoretically bypass this limitation under steady-state conditions, the perturbation introduced by CHX alters global protein levels, making it very challenging to establish a S that could be reliably compared between perturbed and unperturbed states. In fact, the global protein levels dictate the normalization of the computed S.[19,84] This limitation should also be considered when analyzing LFQ data. Additionally, owing to the anticipated global effects of CHX, canonical dSILAC cannot be employed outside of a steady state to separately compute S and k.[19,69] Finally, since each data point represents a distinct sample, determining the cell division rate through cell counting during the experimental time course is challenging.

To analyze the dSILAC data, we fitted the percentage of light (%L) decay to a single mono-exponential decay model,[70] retaining only those proteins for which this model demonstrated a sufficiently good fit ($R^2 > 0.9$) in our subsequent analysis. Current literature[85,86] indicates that a significant number of proteins exhibit non-exponential or multi-exponential decay behaviors. However, note that this does not affect our model predictions, as multi-exponential decay can be decomposed into a sum of mono-exponential decays.

The primary limitation of our passive adaptation model is also its greatest strength—its simplicity and parsimony. The model is constructed using linear, ordinary differential equations, thus not accounting for stochastic effects or non-linear dependencies on protein concentrations. Despite this, the passive adaptation model is adequate for recapitulating and predicting the data we obtained.

Finally, we acknowledge that we did not precisely measure cell volume in our imaging experiments, which limits our ability to compare our data with findings from studies focused on mammalian cell volume. We believe that accurately measuring cell volume could help bridge different areas of knowledge and pave the way toward a better understanding of the growth laws governing mammalian cells.

RESOURCE AVAILABILITY

Lead contact

Requests for further information and resource sharing and reagents should be directed to and will be fulfilled by the lead contact, David Suter (david.suter@epfl.ch).

Materials availability

Plasmids and cell lines generated in this study are available upon request to the lead contact.

Data and code availability

LFQ proteomics were deposited on PRIDE under accession number PXD056601. dSILAC proteomics data for NIH/3T3 cells were deposited on PRIDE under accession number PXD061384. dSILAC proteomics data for mESCs were deposited on PRIDE under accession number PXD061306. RNA-seq data were deposited under accession number GSE278929. All original codes for reproducing analyses of this paper have been deposited on GitHub and are publicly available (DOI: 10.5281/zenodo.17283838). Namely, key scripts for data analysis—inference algorithm and cell segmentation/fluorescence quantification, RNA-seq, and dSILAC analyses along with dSILAC data—have been deposited on GitHub: https://github.com/UPSUTER/ProTuCo. Imaging data or other data reported in this paper are available from the lead contact upon request. Any additional information required to reanalyze the data reported in this paper is available from the lead contact upon request.

ACKNOWLEDGMENTS

This work was supported by EPFL core funding and the Synapsis Foundation Switzerland. The authors want to thank Almut Eisele, Felix Naef, and Maike Hansen for their careful reading of the manuscript and their comments. We would like to thank Louis-Alexandre Ongaro for testing the feasibility of the astrocyte differentiation protocol and performing the initial differentiation to astrocyte progenitors. Fluorescence-activated cell sorting was performed at the EPFL Flow Cytometry Core Facility (EPFL-FCCF). Microscopy and image analysis were performed using the resources of the EPFL Bioimaging and Optics Core Facility (EPFL-BIOP). Mass spectrometry was performed at the

Proteomics Core Facility (EPFL-PCF). We particularly thank Maria Pavlou and Mathilde Willemin for sharing their expertise in mass spectrometry.

AUTHOR CONTRIBUTIONS

Conceptualization, M.S.S., B.M., and D.M.S.; methodology, M.S.S., B.M., and D.M.S.; software, B.M.; validation, B.M., J.D., and C.D.; formal analysis, M.S.S., B.M., and E.L.; investigation, M.S.S., B.M., J.D., E.L., and C.D.; data curation, M.S.S. and B.M.; writing – original draft, M.S.S., B.M., and D.M.S.; writing – review and editing, B.M., J.D., E.L., and D.M.S.; visualization, B.M.; supervision, D.M.S.; and funding acquisition, D.M.S.

DECLARATION OF INTERESTS

The authors declare no competing interests.

STAR★METHODS

Detailed methods are provided in the online version of this paper and include the following:

- KEY RESOURCES TABLE
- EXPERIMENTAL MODEL AND STUDY PARTICIPANT DETAILS
  - Cell Culture
- METHOD DETAILS
  - Production of lentiviral vectors and generation of stable cell lines
  - Generation of the mESC SLT knock-in cell line
  - Generation of the hESC SLT knock-in cell line
  - Generation of hESC-derived neurons (iNGNs)
  - Differentiation of hESCs into astrocytes
  - Immunofluorescence for characterization of astrocyte-enriched cell culture
  - Immunofluorescence for characterization of hESC-derived neurons (iNGN)
  - Immunofluorescence for characterization of pluripotency of mESC
  - Snapshot imaging of the MCFT upon CHX/MYCi/INK128 steady-state treatments
  - Snapshot imaging of the MCFT upon steady-state amino acids depletion
  - Live imaging of the MCFT upon CHX treatment/release
  - Live imaging of the MCFT upon MYCi treatment/release
  - SNAP-tag pulse-chase labeling
  - Dox pulse-chase experiment
  - Flow cytometry
  - Imbalance computation
  - *N*-Hydroxysuccinimide (NHS ester) labeling and imaging
  - HPG labelling in iNGNs
  - ELISA for p70S6K
  - Proteasome-Glo assay
  - RNA-seq
  - Label-free Mass Spectrometry experiments
  - Dynamic SILAC
  - Image pre-processing
  - Cell segmentation and tracking
  - Quantification of k and k_{deg} from SNAP pulse-chase labeling
  - Quantification of S and k from the MCFT
  - Quantification of k_{dil} from time-lapse movies
  - Modeling and inference from MCFT traces
  - Modeling and inference from SNAP trajectories
  - Log-likelihood and bootstrapping for model selection
- QUANTIFICATION AND STATISTICAL ANALYSIS
- ETHICS STATEMENT

SUPPLEMENTAL INFORMATION

Supplemental information can be found online at https://doi.org/10.1016/j.cels.2025.101456.

Received: April 2, 2025
Revised: August 19, 2025
Accepted: October 31, 2025
Published: December 22, 2025

REFERENCES

1. Dikic, I., and Elazar, Z. (2018). Mechanism and medical implications of mammalian autophagy. Nat. Rev. Mol. Cell Biol. *19*, 349–364. https://doi.org/10.1038/s41580-018-0003-4.
2. Balakrishnan, R., Mori, M., Segota, I., Zhang, Z., Aebersold, R., Ludwig, C., and Hwa, T. (2022). Principles of gene regulation quantitatively connect DNA to RNA and proteins in bacteria. Science *378*, eabk2066. https://doi.org/10.1126/science.abk2066.
3. Seinkmane, E., Edmondson, A., Peak-Chew, S.Y., Zeng, A., Rzechorzek, N.M., James, N.R., West, J., Munns, J., Wong, D.C., Beale, A.D., et al. (2022). Circadian regulation of protein turnover and proteome renewal. Preprint at bioRxiv. https://doi.org/10.1101/2022.09.30.509905.
4. Klein, M.E., Castillo, P.E., and Jordan, B.A. (2015). Coordination between Translation and Degradation Regulates Inducibility of mGluR-LTD. Cell Rep. *10*, 1459–1466. https://doi.org/10.1016/j.celrep.2015.02.020.
5. Ramachandran, K.V., Fu, J.M., Schaffer, T.B., Na, C.H., Delannoy, M., and Margolis, S.S. (2018). Activity-Dependent Degradation of the Nascentome by the Neuronal Membrane Proteasome. Mol. Cell *71*, 169–177.e6. https://doi.org/10.1016/j.molcel.2018.06.013.
6. Kristensen, A.R., Gsponer, J., and Foster, L.J. (2013). Protein synthesis rate is the predominant regulator of protein expression during differentiation. Mol. Syst. Biol. *9*, 689. https://doi.org/10.1038/msb.2013.47.
7. Honda, T., Cremer, J., Mancini, L., Zhang, Z., Pilizota, T., and Hwa, T. (2022). Coordination of gene expression with cell size enables Escherichia coli to efficiently maintain motility across conditions. Proc. Natl. Acad. Sci. USA *119*, e2110342119. https://doi.org/10.1073/pnas.2110342119.
8. Liu, S., Tan, C., Melo-Gavin, C., Ginzberg, M.B., Blutrich, R., Patel, N., Rape, M., Mark, K.G., and Kafri, R. (2021). Large cells activate global protein degradation to maintain cell size homeostasis. Preprint at bioRxiv. https://doi.org/10.1101/2021.11.09.467936.
9. Motil, K.J., Matthews, D.E., Bier, D.M., Burke, J.F., Munro, H.N., and Young, V.R. (1981). Whole-body leucine and lysine metabolism: response to dietary protein intake in young men. Am. J. Physiol. *240*, E712–E721. https://doi.org/10.1152/ajpendo.1981.240.6.E712.
10. Wu, C.-l., and Wen, H. (2020). Heightened protein-translation activities in mammalian cells and the disease/treatment implications. Natl. Sci. Rev. *7*, 1851–1855. https://doi.org/10.1093/nsr/nwaa066.
11. Wolfe, R.R. (2001). Effects of amino acid intake on anabolic processes. Can. J. Appl. Physiol. *26*, S220–S227. https://doi.org/10.1139/h2001-056.
12. Graber, T.G., Borack, M.S., Reidy, P.T., Volpi, E., and Rasmussen, B.B. (2017). Essential amino acid ingestion alters expression of genes associated with amino acid sensing, transport, and mTORC1 regulation in human skeletal muscle. Nutr. Metab. *14*, 35. https://doi.org/10.1186/s12986-017-0187-1.
13. Chen, X., Haribowo, A.G., Baik, A.H., Fossati, A., Stevenson, E., Chen, Y.R., Reyes, N.S., Peng, T., Matthay, M.A., Traglia, M., et al. (2023). In vivo protein turnover rates in varying oxygen tensions nominate MYBBP1A as a mediator of the hyperoxia response. Sci. Adv. *9*, eadj4884. https://doi.org/10.1126/sciadv.adj4884.
14. Sørensen, B.S., Busk, M., Overgaard, J., Horsman, M.R., and Alsner, J. (2015). Simultaneous Hypoxia and Low Extracellular pH Suppress Overall Metabolic Rate and Protein Synthesis In Vitro. PLoS One *10*, e0134955. https://doi.org/10.1371/journal.pone.0134955.
15. Rennie, M.J., Edwards, R.H., Halliday, D., Matthews, D.E., Wolman, S.L., and Millward, D.J. (1982). Muscle protein synthesis measured by stable isotope techniques in man: the effects of feeding and fasting. Clin. Sci. *63*, 519–523. https://doi.org/10.1042/cs0630519.

16. Signer, R.A.J., Magee, J.A., Salic, A., and Morrison, S.J. (2014). Haematopoietic stem cells require a highly regulated protein synthesis rate. Nature *509*, 49–54. https://doi.org/10.1038/nature13035.

17. Magee, J.A., and Signer, R.A.J. (2021). Developmental Stage-Specific Changes in Protein Synthesis Differentially Sensitize Hematopoietic Stem Cells and Erythroid Progenitors to Impaired Ribosome Biogenesis. Stem Cell Rep. *16*, 20–28. https://doi.org/10.1016/j.stemcr.2020.11.017.

18. Huang, Y., Urban, C., Hubel, P., Stukalov, A., and Pichlmair, A. (2024). Protein turnover regulation is critical for influenza A virus infection. Cell Syst. *15*, 911–929.e8. https://doi.org/10.1016/j.cels.2024.09.004.

19. Jovanovic, M., Rooney, M.S., Mertins, P., Przybylski, D., Chevrier, N., Satija, R., Rodriguez, E.H., Fields, A.P., Schwartz, S., Raychowdhury, R., et al. (2015). Immunogenetics. Dynamic profiling of the protein life cycle in response to pathogens. Science *347*, 1259038. https://doi.org/10.1126/science.1259038.

20. Balch, W.E., Morimoto, R.I., Dillin, A., and Kelly, J.W. (2008). Adapting proteostasis for disease intervention. Science *319*, 916–919. https://doi.org/10.1126/science.1141448.

21. Hipp, M.S., Kasturi, P., and Hartl, F.U. (2019). The proteostasis network and its decline in ageing. Nat. Rev. Mol. Cell Biol. *20*, 421–435. https://doi.org/10.1038/s41580-019-0101-y.

22. Buchberger, A., Bukau, B., and Sommer, T. (2010). Protein quality control in the cytosol and the endoplasmic reticulum: brothers in arms. Mol. Cell *40*, 238–252. https://doi.org/10.1016/j.molcel.2010.10.001.

23. Klaips, C.L., Jayaraj, G.G., and Hartl, F.U. (2018). Pathways of cellular proteostasis in aging and disease. J. Cell Biol. *217*, 51–63. https://doi.org/10.1083/jcb.201709072.

24. Pakos-Zebrucka, K., Koryga, I., Mnich, K., Ljujic, M., Samali, A., and Gorman, A.M. (2016). The integrated stress response. EMBO Rep. *17*, 1374–1395. https://doi.org/10.15252/embr.201642195.

25. Arimoto, K., Fukuda, H., Imajoh-Ohmi, S., Saito, H., and Takekawa, M. (2008). Formation of stress granules inhibits apoptosis by suppressing stress-responsive MAPK pathways. Nat. Cell Biol. *10*, 1324–1332. https://doi.org/10.1038/ncb1791.

26. He, L., Cho, S., and Blenis, J. (2025). mTORC1, the maestro of cell metabolism and growth. Genes Dev. *39*, 109–131. https://doi.org/10.1101/gad.352084.124.

27. Zhao, J., Zhai, B., Gygi, S.P., and Goldberg, A.L. (2015). mTOR inhibition activates overall protein degradation by the ubiquitin proteasome system as well as by autophagy. Proc. Natl. Acad. Sci. USA *112*, 15790–15797. https://doi.org/10.1073/pnas.1521919112.

28. Cui, D.S., Webster, S.M., and Davis, J.H. (2024). Integrated proteasomal and lysosomal activity shape mTOR-regulated proteome remodeling. Preprint at bioRxiv. https://doi.org/10.1101/2024.07.20.603815.

29. Zhang, Y., Nicholatos, J., Dreier, J.R., Ricoult, S.J.H., Widenmaier, S.B., Hotamisligil, G.S., Kwiatkowski, D.J., and Manning, B.D. (2014). Coordinated regulation of protein synthesis and degradation by mTORC1. Nature *513*, 440–443. https://doi.org/10.1038/nature13492.

30. Neurohr, G.E., Terry, R.L., Lengefeld, J., Bonney, M., Brittingham, G.P., Moretto, F., Miettinen, T.P., Vaites, L.P., Soares, L.M., Paulo, J.A., et al. (2019). Excessive Cell Growth Causes Cytoplasm Dilution And Contributes to Senescence. Cell *176*, 1083–1097.e18. https://doi.org/10.1016/j.cell.2019.01.018.

31. Alber, A.B., Paquet, E.R., Biserni, M., Naef, F., and Suter, D.M. (2018). Single Live Cell Monitoring of Protein Turnover Reveals Intercellular Variability and Cell-Cycle Dependence of Degradation Rates. Mol. Cell *71*, 1079–1091.e9. https://doi.org/10.1016/j.molcel.2018.07.023.

32. Barry, J.D., Donà, E., Gilmour, D., and Huber, W. (2016). TimerQuant: a modelling approach to tandem fluorescent timer design and data interpretation for measuring protein turnover in embryos. Development *143*, 174–179. https://doi.org/10.1242/dev.125971.

33. Khmelinskii, A., Keller, P.J., Bartosik, A., Meurer, M., Barry, J.D., Mardin, B.R., Kaufmann, A., Trautmann, S., Wachsmuth, M., Pereira, G., et al. (2012). Tandem fluorescent protein timers for in vivo analysis of protein dynamics. Nat. Biotechnol. *30*, 708–714. https://doi.org/10.1038/nbt.2281.

34. Alber, A.B., and Suter, D.M. (2018). Single-Cell Quantification of Protein Degradation Rates by Time-Lapse Fluorescence Microscopy in Adherent Cell Culture. J. Vis. Exp. 56604. https://doi.org/10.3791/56604.

35. Bodor, D.L., Rodríguez, M.G., Moreno, N., and Jansen, L.E.T. (2012). Chapter 8. Analysis of protein turnover by quantitative SNAP-based pulse-chase imaging. Curr. Protoc. Cell Biol. *Chapter*, Unit8.8. https://doi.org/10.1002/0471143030.cb0808s55.

36. Woodside, K.H. (1976). Effects of cycloheximide on protein degradation and gluconeogenesis in the perfused rat liver. Biochim. Biophys. Acta *421*, 70–79. https://doi.org/10.1016/0304-4165(76)90170-7.

37. Beugnet, A., Tee, A.R., Taylor, P.M., and Proud, C.G. (2003). Regulation of targets of mTOR (mammalian target of rapamycin) signalling by intracellular amino acid availability. Biochem. J. *372*, 555–566. https://doi.org/10.1042/BJ20021266.

38. Nandi, D., Woodward, E., Ginsburg, D.B., and Monaco, J.J. (1997). Intermediates in the formation of mouse 20S proteasomes: implications for the assembly of precursor beta subunits. EMBO J. *16*, 5363–5375. https://doi.org/10.1093/emboj/16.17.5363.

39. Khan, S., van den Broek, M., Schwarz, K., de Giuli, R., Diener, P.A., and Groettrup, M. (2001). Immunoproteasomes largely replace constitutive proteasomes during an antiviral and antibacterial immune response in the liver. J. Immunol. *167*, 6859–6868. https://doi.org/10.4049/jimmunol.167.12.6859.

40. Tanaka, K., and Ichihara, A. (1989). Half-life of proteasomes (multiprotease complexes) in rat liver. Biochem. Biophys. Res. Commun. *159*, 1309–1315. https://doi.org/10.1016/0006-291x(89)92253-5.

41. Cuervo, A.M., Palmer, A., Rivett, A.J., and Knecht, E. (1995). Degradation of proteasomes by lysosomes in rat liver. Eur. J. Biochem. *227*, 792–800. https://doi.org/10.1111/j.1432-1033.1995.tb20203.x.

42. Jha, R.K., Kouzine, F., and Levens, D. (2023). MYC function and regulation in physiological perspective. Front. Cell Dev. Biol. *11*, 1268275. https://doi.org/10.3389/fcell.2023.1268275.

43. Huang, M.-J., Cheng, Y.C., Liu, C.-R., Lin, S., and Liu, H.E. (2006). A small-molecule c-Myc inhibitor, 10058-F4, induces cell-cycle arrest, apoptosis, and myeloid differentiation of human acute myeloid leukemia. Exp. Hematol. *34*, 1480–1489. https://doi.org/10.1016/j.exphem.2006.06.019.

44. Schwanhäusser, B., Busse, D., Li, N., Dittmar, G., Schuchhardt, J., Wolf, J., Chen, W., and Selbach, M. (2011). Global quantification of mammalian gene expression control. Nature *473*, 337–342. https://doi.org/10.1038/nature10098.

45. Cerbini, T., Funahashi, R., Luo, Y., Liu, C., Park, K., Rao, M., Malik, N., and Zou, J. (2015). Transcription activator-like effector nuclease (TALEN)-mediated CLYBL targeting enables enhanced transgene expression and one-step generation of dual reporter human induced pluripotent stem cell (iPSC) and neural stem cell (NSC) lines. PLoS One *10*, e0116032. https://doi.org/10.1371/journal.pone.0116032.

46. Ramos-Gonzalez, P., Mato, S., Chara, J.C., Verkhratsky, A., Matute, C., and Cavaliere, F. (2021). Astrocytic atrophy as a pathological feature of Parkinson's disease with LRRK2 mutation. NPJ Parkinsons. Dis. *7*, 31. https://doi.org/10.1038/s41531-021-00175-w.

47. Metzner, C., Mark, C., Steinwachs, J., Lautscham, L., Stadler, F., and Fabry, B. (2015). Superstatistical analysis and modelling of heterogeneous random walks. Nat. Commun. *6*, 7516. https://doi.org/10.1038/ncomms8516.

48. Mark, C., Metzner, C., Lautscham, L., Strissel, P.L., Strick, R., and Fabry, B. (2018). Bayesian model selection for complex dynamic systems. Nat. Commun. *9*, 1803. https://doi.org/10.1038/s41467-018-04241-5.

49. Mark, C., Metzner, C., and Fabry, B. (2014). Bayesian Inference of Time Varying Parameters in Autoregressive Processes. Preprint at arXiv. https://doi.org/10.48550/arXiv.1405.1668.

50. Martin, B., and Suter, D.M. (2023). An out-of-equilibrium definition of protein turnover. BioEssays *45*, e2200209. https://doi.org/10.1002/bies.202200209.

51. Padgett, J., and Santos, S.D.M. (2020). From clocks to dominoes: lessons on cell cycle remodelling from embryonic stem cells. FEBS Lett. https://doi.org/10.1002/1873-3468.13862.

52. Zatulovskiy, E., Zhang, S., Berenson, D.F., Topacio, B.R., and Skotheim, J.M. (2020). Cell growth dilutes the cell cycle inhibitor Rb to trigger cell division. Science *369*, 466–471. https://doi.org/10.1126/science.aaz6213.

53. Perez-Pinera, P., Ousterout, D.G., Brown, M.T., and Gersbach, C.A. (2012). Gene targeting to the ROSA26 locus directed by engineered zinc finger nucleases. Nucleic Acids Res. *40*, 3741–3752. https://doi.org/10.1093/nar/gkr1214.

54. Hara, K., Yonezawa, K., Weng, Q.P., Kozlowski, M.T., Belham, C., and Avruch, J. (1998). Amino acid sufficiency and mTOR regulate p70 S6 kinase and eIF-4E BP1 through a common effector mechanism. J. Biol. Chem. *273*, 14484–14494. https://doi.org/10.1074/jbc.273.23.14484.

55. Nielsen, P.J., Manchester, K.L., Towbin, H., Gordon, J., and Thomas, G. (1982). The phosphorylation of ribosomal protein S6 in rat tissues following cycloheximide injection, in diabetes, and after denervation of diaphragm. A simple immunological determination of the extent of S6 phosphorylation on protein blots. J. Biol. Chem. *257*, 12316–12321. https://doi.org/10.1016/S0021-9258(18)33716-5.

56. Price, D.J., Nemenoff, R.A., and Avruch, J. (1989). Purification of a hepatic S6 kinase from cycloheximide-treated Rats. J. Biol. Chem. *264*, 13825–13833. https://doi.org/10.1016/S0021-9258(18)80075-8.

57. Shah, O.J., Anthony, J.C., Kimball, S.R., and Jefferson, L.S. (2000). 4E-BP1 and S6K1: translational integration sites for nutritional and hormonal information in muscle. Am. J. Physiol., Endocrinol. Metab. *279*, E715–E729. https://doi.org/10.1152/ajpendo.2000.279.4.E715.

58. Proud, C.G. (2004). mTOR-mediated regulation of translation factors by amino acids. Biochem. Biophys. Res. Commun. *313*, 429–436. https://doi.org/10.1016/j.bbrc.2003.07.015.

59. Watanabe-Asano, T., Kuma, A., and Mizushima, N. (2014). Cycloheximide inhibits starvation-induced autophagy through mTORC1 activation. Biochem. Biophys. Res. Commun. *445*, 334–339. https://doi.org/10.1016/j.bbrc.2014.01.180.

60. Xu, Y., Parmar, A., Roux, E., Balbis, A., Dumas, V., Chevalier, S., and Posner, B.I. (2012). Epidermal growth factor-induced vacuolar (H+)-atpase assembly: a role in signaling via mTORC1 activation. J. Biol. Chem. *287*, 26409–26422. https://doi.org/10.1074/jbc.M112.352229.

61. Finlay, D., Ruiz-Alcaraz, A.J., Lipina, C., Perrier, S., and Sutherland, C. (2006). A temporal switch in the insulin-signalling pathway that regulates hepatic IGF-binding protein-1 gene expression. J. Mol. Endocrinol. *37*, 227–237. https://doi.org/10.1677/jme.1.02084.

62. Schmitz, F., Heit, A., Dreher, S., Eisenächer, K., Mages, J., Haas, T., Krug, A., Janssen, K.-P., Kirschning, C.J., and Wagner, H. (2008). Mammalian target of rapamycin (mTOR) orchestrates the defense program of innate immune cells. Eur. J. Immunol. *38*, 2981–2992. https://doi.org/10.1002/eji.200838761.

63. Bar-Peled, L., and Sabatini, D.M. (2014). Regulation of mTORC1 by amino acids. Trends Cell Biol. *24*, 400–406. https://doi.org/10.1016/j.tcb.2014.03.003.

64. Laplante, M., and Sabatini, D.M. (2013). Regulation of mTORC1 and its impact on gene expression at a glance. J. Cell Sci. *126*, 1713–1719. https://doi.org/10.1242/jcs.125773.

65. Hussein, A.M., Wang, Y., Mathieu, J., Margaretha, L., Song, C., Jones, D.C., Cavanaugh, C., Miklas, J.W., Mahen, E., Showalter, M.R., et al. (2020). Metabolic Control over mTOR-Dependent Diapause-like State. Dev. Cell *52*, 236–250.e7. https://doi.org/10.1016/j.devcel.2019.12.018.

66. Bulut-Karslioglu, A., Biechele, S., Jin, H., Macrae, T.A., Hejna, M., Gertsenstein, M., Song, J.S., and Ramalho-Santos, M. (2016). Inhibition of mTor induces a paused pluripotent state. Nature *540*, 119–123. https://doi.org/10.1038/nature20578.

67. Roux, P.P., and Topisirovic, I. (2018). Signaling Pathways Involved in the Regulation of mRNA Translation. Mol. Cell. Biol. *38*, e00070. –e00018. https://doi.org/10.1128/MCB.00070-18.

68. Dörrbaum, A.R., Kochen, L., Langer, J.D., and Schuman, E.M. (2018). Local and global influences on protein turnover in neurons and glia. eLife *7*, e34202. https://doi.org/10.7554/eLife.34202.

69. Dörrbaum, A.R., Alvarez-Castelao, B., Nassim-Assir, B., Langer, J.D., and Schuman, E.M. (2020). Proteome dynamics during homeostatic scaling in cultured neurons. eLife *9*, e52939. https://doi.org/10.7554/eLife.52939.

70. Dörrbaum, A.R., Schuman, E.M., and Langer, J.D. (2023). Dynamic SILAC to Determine Protein Turnover in Neurons and Glia. In SILAC: Methods and Protocols, J.L. Luque-Garcia, ed. (Springer), pp. 1–17. https://doi.org/10.1007/978-1-0716-2863-8_1.

71. Amenta, J.S., Sargus, M.J., and Baccino, F.M. (1978). Inhibition of basal protein degradation in rat embryo fibroblasts by cycloheximide: correlation with activities of lysosomal proteases. J. Cell. Physiol. *97*, 267–283. https://doi.org/10.1002/jcp.1040970302.

72. Welle, K.A., Zhang, T., Hryhorenko, J.R., Shen, S., Qu, J., and Ghaemmaghami, S. (2016). Time-resolved Analysis of Proteome Dynamics by Tandem Mass Tags and Stable Isotope Labeling in Cell Culture (TMT-SILAC) Hyperplexing. Mol. Cell. Proteomics *15*, 3551–3563. https://doi.org/10.1074/mcp.M116.063230.

73. Liu, S., Tan, C., Melo-Gavin, C., Ginzberg, M.B., Blutrich, R., Patel, N., Rape, M., Mark, K.G., and Kafri, R. (2025). Oversized cells activate global proteasome-mediated protein degradation to maintain cell size homeostasis. eLife *14*, e75393. https://doi.org/10.7554/eLife.75393.

74. Ginzberg, M.B., Chang, N., D'Souza, H., Patel, N., Kafri, R., and Kirschner, M.W. (2018). Cell size sensing in animal cells coordinates anabolic growth rates and cell cycle progression to maintain cell size uniformity. eLife *7*, e26957. https://doi.org/10.7554/eLife.26957.

75. Nichols, J., and Smith, A. (2009). Naive and primed pluripotent states. Cell Stem Cell *4*, 487–492. https://doi.org/10.1016/j.stem.2009.05.015.

76. Chen, C., Zhang, X., Wang, Y., Chen, X., Chen, W., Dan, S., She, S., Hu, W., Dai, J., Hu, J., et al. (2022). Translational and post-translational control of human naïve versus primed pluripotency. iScience *25*, 103645. https://doi.org/10.1016/j.isci.2021.103645.

77. Alhasan, B.A., Gordeev, S.A., Knyazeva, A.R., Aleksandrova, K.V., Margulis, B.A., Guzhova, I.V., and Suvorova, I.I. (2021). The mTOR Pathway in Pluripotent Stem Cells: Lessons for Understanding Cancer Cell Dormancy. Membranes *11*, 858. https://doi.org/10.3390/membranes11110858.

78. Todorova, P.K., Jackson, B.T., Garg, V., Paras, K.I., Brunner, J.S., Bridgeman, A.E., Chen, Y., Baksh, S.C., Yan, J., Hadjantonakis, A.-K., et al. (2024). Amino acid intake strategies define pluripotent cell states. Nat. Metab. *6*, 127–140. https://doi.org/10.1038/s42255-023-00940-6.

79. Whitten, W.K., and Biggers, J.D. (1968). Complete development in vitro of the pre-implantation stages of the mouse in a simple chemically defined medium. J. Reprod. Fertil. *17*, 399–401. https://doi.org/10.1530/jrf.0.0170399.

80. Miao, Y., Du, Q., Zhang, H.-G., Yuan, Y., Zuo, Y., and Zheng, H. (2023). Cycloheximide (CHX) Chase Assay to Examine Protein Half-life. Bio-Protoc. *13*, e4690. https://doi.org/10.21769/BioProtoc.4690.

81. Diaz-Cuadros, M., Miettinen, T.P., Sheedy, D., Díaz-García, C.M., Gapon, S., Hubaud, A., Yellen, G., Manalis, S.R., Oldham, W., and Pourquié, O. (2021). Metabolic regulation of species-specific developmental rates. Preprint at bioRxiv. https://doi.org/10.1101/2021.08.27.457974.

82. Matsuda, M., Hayashi, H., Garcia-Ojalvo, J., Yoshioka-Kobayashi, K., Kageyama, R., Yamanaka, Y., Ikeya, M., Toguchida, J., Alev, C., and Ebisuya, M. (2020). Species-specific segmentation clock periods are due to differential biochemical reaction speeds. Science *369*, 1450–1455. https://doi.org/10.1126/science.aba7668.

83. Rayon, T., Stamataki, D., Perez-Carrasco, R., Garcia-Perez, L., Barrington, C., Melchionda, M., Exelby, K., Lazaro, J., Tybulewicz, V.L.J., Fisher, E.M.C., et al. (2020). Species-specific pace of development is associated with differences in protein stability. Science *369*, eaba7667. https://doi.org/10.1126/science.aba7667.

84. Ross, A.B., Langer, J.D., and Jovanovic, M. (2021). Proteome Turnover in the Spotlight: Approaches, Applications, and Perspectives. Mol. Cell. Proteomics *20*, 100016. https://doi.org/10.1074/mcp.R120.002190.

85. McShane, E., Sin, C., Zauber, H., Wells, J.N., Donnelly, N., Wang, X., Hou, J., Chen, W., Storchova, Z., Marsh, J.A., et al. (2016). Kinetic Analysis of Protein Stability Reveals Age-Dependent Degradation. Cell *167*, 803–815.e21. https://doi.org/10.1016/j.cell.2016.09.015.

86. Meadow, M.E., Broas, S., Hoare, M., Alimohammadi, F., Welle, K.A., Swovick, K., Hryhorenko, J.R., Martinez, J.C., Biashad, S.A., Seluanov, A., et al. (2024). Proteome Birthdating Reveals Age-Selectivity of Protein Ubiquitination. Mol. Cell. Proteomics *23*, 100791. https://doi.org/10.1016/j.mcpro.2024.100791.

87. Suter, D.M., Cartier, L., Bettiol, E., Tirefort, D., Jaconi, M.E., Dubois-Dauphin, M., and Krause, K.-H. (2006). Rapid generation of stable transgenic embryonic stem cell lines using modular lentivectors. Stem Cells *24*, 615–623. https://doi.org/10.1634/stemcells.2005-0226.

88. Deluz, C., Friman, E.T., Strebinger, D., Benke, A., Raccaud, M., Callegari, A., Leleu, M., Manley, S., and Suter, D.M. (2016). A role for mitotic bookmarking of SOX2 in pluripotency and differentiation. Genes Dev. *30*, 2538–2550. https://doi.org/10.1101/gad.289256.116.

89. Kasparek, P., Krausova, M., Haneckova, R., Kriz, V., Zbodakova, O., Korinek, V., and Sedlacek, R. (2014). Efficient gene targeting of the Rosa26 locus in mouse zygotes using TALE nucleases. FEBS Lett. *588*, 3982–3988. https://doi.org/10.1016/j.febslet.2014.09.014.

90. Sauter, E.J., Kutsche, L.K., Klapper, S.D., and Busskamp, V. (2019). Induced Neurons for the Study of Neurodegenerative and Neurodevelopmental Disorders. In Fragile-X Syndrome: Methods and Protocols, D. Ben-Yosef and Y. Mayshar, eds. (Springer), pp. 101–121. https://doi.org/10.1007/978-1-4939-9080-1_9.

91. Cajka, G., Liu, M., and Shalem, O. (2024). CRISPR associated enzymes are mislocalized to the cytoplasm in iPSC-derived neurons resulting in KRAB-specific degradation. Preprint at bioRxiv. https://doi.org/10.1101/2024.10.19.619045.

92. Dobin, A., Davis, C.A., Schlesinger, F., Drenkow, J., Zaleski, C., Jha, S., Batut, P., Chaisson, M., and Gingeras, T.R. (2013). STAR: ultrafast universal RNA-seq aligner. Bioinformatics *29*, 15–21. https://doi.org/10.1093/bioinformatics/bts635.

93. Love, M.I., Huber, W., and Anders, S. (2014). Moderated estimation of fold change and dispersion for RNA-seq data with DESeq2. Genome Biol. *15*, 550. https://doi.org/10.1186/s13059-014-0550-8.

94. R Core Team (2023). R: A Language and Environment for Statistical Computing (R Foundation for Statistical Computing).

95. Tweedie, S., Braschi, B., Gray, K., Jones, T.E.M., Seal, R.L., Yates, B., and Bruford, E.A. (2021). Genenames.org: the HGNC and VGNC resources in 2021. Nucleic Acids Res. *49*, D939–D946. https://doi.org/10.1093/nar/gkaa980.

96. Rath, S., Sharma, R., Gupta, R., Ast, T., Chan, C., Durham, T.J., Goodman, R.P., Grabarek, Z., Haas, M.E., Hung, W.H.W., et al. (2021). MitoCarta3.0: an updated mitochondrial proteome now with sub-organelle localization and pathway annotations. Nucleic Acids Res. *49*, D1541–D1547. https://doi.org/10.1093/nar/gkaa1011.

97. Wiśniewski, J.R., Zougman, A., Nagaraj, N., and Mann, M. (2009). Universal sample preparation method for proteome analysis. Nat. Methods *6*, 359–362. https://doi.org/10.1038/nmeth.1322.

98. Kulak, N.A., Pichler, G., Paron, I., Nagaraj, N., and Mann, M. (2014). Minimal, encapsulated proteomic-sample processing applied to copy-number estimation in eukaryotic cells. Nat. Methods *11*, 319–324. https://doi.org/10.1038/nmeth.2834.

99. Cox, J., and Mann, M. (2008). MaxQuant enables high peptide identification rates, individualized p.p.b.-range mass accuracies and proteome-wide protein quantification. Nat. Biotechnol. *26*, 1367–1372. https://doi.org/10.1038/nbt.1511.

100. Cox, J., Hein, M.Y., Luber, C.A., Paron, I., Nagaraj, N., and Mann, M. (2014). Accurate proteome-wide label-free quantification by delayed normalization and maximal peptide ratio extraction, termed MaxLFQ. Mol. Cell. Proteomics *13*, 2513–2526. https://doi.org/10.1074/mcp.M113.031591.

101. Tyanova, S., Temu, T., Sinitcyn, P., Carlson, A., Hein, M.Y., Geiger, T., Mann, M., and Cox, J. (2016). The Perseus computational platform for comprehensive analysis of (prote)omics data. Nat. Methods *13*, 731–740. https://doi.org/10.1038/nmeth.3901.

102. Bendall, S.C., Hughes, C., Stewart, M.H., Doble, B., Bhatia, M., and Lajoie, G.A. (2008). Prevention of amino acid conversion in SILAC experiments with embryonic stem cells. Mol. Cell. Proteomics *7*, 1587–1597. https://doi.org/10.1074/mcp.M800113-MCP200.

103. Ershov, D., Phan, M.-S., Pylvänäinen, J.W., Rigaud, S.U., Le Blanc, L., Charles-Orszag, A., Conway, J.R.W., Laine, R.F., Roy, N.H., Bonazzi, D., et al. (2022). TrackMate 7: integrating state-of-the-art segmentation algorithms into tracking pipelines. Nat. Methods *19*, 829–832. https://doi.org/10.1038/s41592-022-01507-1.

104. Weigert, M., Schmidt, U., Haase, R., Sugawara, K., and Myers, G. (2020). Star-convex Polyhedra for 3D Object Detection and Segmentation in Microscopy. In IEEE Winter Conference on Applications of Computer Vision (WACV), pp. 3655–3662. https://doi.org/10.1109/WACV45572.2020.9093435.

105. Munkres, J. (1957). Algorithms for the Assignment and Transportation Problems. J. Soc. Ind. Appl. Math. *5*, 32–38. https://doi.org/10.1137/0105003.

106. Savitzky, A., and Golay, M.J.E. (1964). Smoothing and Differentiation of Data by Simplified Least Squares Procedures. Anal. Chem. *36*, 1627–1639. https://doi.org/10.1021/ac60214a047.

107. Pachitariu, M., and Stringer, C. (2022). Cellpose 2.0: how to train your own model. Nat. Methods *19*, 1634–1641. https://doi.org/10.1038/s41592-022-01663-4.

108. Witz, G. (2024). https://github.com/guiwitz/microfilm.

109. Fischler, M.A., and Bolles, R.C. (1981). Random sample consensus: a paradigm for model fitting with applications to image analysis and automated cartography. Commun. ACM *24*, 381–395. https://doi.org/10.1145/358669.358692.

110. Pedregosa, F., Varoquaux, G., Gramfort, A., Michel, V., Thirion, B., Grisel, O., Blondel, M., Prettenhofer, P., Weiss, R., Dubourg, V., et al. (2011). Scikit-learn: Machine Learning in Python. J. Mach. Learn. Res. *12*, 2825–2830.

STAR★METHODS

KEY RESOURCES TABLE

REAGENT or RESOURCE	SOURCE	IDENTIFIER
Antibodies		
Anti-Ki67	BD Biosciences	Cat# 550609; RRID: AB_393778
Anti-GFAP	STEMCELL Technologies	Cat# 60048; RRID: AB_3095092
Anti-MAP2	Sigma-Aldrich	Cat# AB5622; RRID: AB_5622
Anti-TUBB	eBioscience	Cat# 14-4510; RRID: AB_2572876
Anti-SOX2	Cell Signaling Technology	Cat# 23064S; RRID: AB_2714146
Anti-NANOG	Thermo Fisher Scientific	Cat# MA5-31459; RRID: AB_2787091
Anti-OCT4	Cell Signaling Technology	Cat# 5677; RRID: AB_10547892
AlexaFluor647 secondary, anti-mouse	Life Technologies	Cat# A31571; RRID: AB_162542
AlexaFluor647 secondary, anti-rabbit	Life Technologies	Cat# A21443; RRID: AB_2535861
Chemicals, peptides, and recombinant proteins		
Dulbecco's Modified Eagle Medium, high glucose, pyruvate	Thermo Fisher Scientific	Cat# 41966029
Fetal Bovine Serum, embryonic stem cell-qualified	Thermo Fisher Scientific	Cat# 16141079
Fetal Bovine Serum	Thermo Fisher Scientific	Cat# 10270106
Sodium pyruvate solution	Sigma-Aldrich	Cat# 113-24-6
Non-essential amino acids	Gibco	Cat# 11140-050
Penicillin/Streptomycin	BioConcept	Cat# 401F00H
L-glutamine (2 mM)	Gibco	Cat# 25030-024
2-mercaptoethanol	Sigma-Aldrich	Cat# 63689
Leukaemia inhibitory factor (LIF)	In-house	N/A
GSK-3 Inhibitor XVI	Merck	Cat# 361559
PD184352	Sigma-Aldrich	Cat# PZ0181
Gelatin	Sigma-Aldrich	Cat# G9391
Trypsin	Sigma-Aldrich	Cat# T4049-100ML
mTeSR Plus	STEMCELL Technologies	Cat# 100-0276
ReLeSR	STEMCELL Technologies	Cat# 05872
Corning Matrigel hESC-qualified matrix	Corning	Cat# 354277
Accutase	Innovative Cell Technology	Cat# AT104
BrainPhys™ Without Phenol-Red	STEMCELL Technologies	Cat# 05791
BrainPhys™ hPSC Neuron Kit	STEMCELL Technologies	Cat# 05795
STEMdiff Astrocyte Maturation Supplement A	STEMCELL Technologies	Cat# 100-0037
STEMdiff Astrocyte Maturation Supplement B	STEMCELL Technologies	Cat# 100-0017
Poly-L-Ornithine (PLO)	Sigma-Aldrich	Cat# P4957
Laminin	Sigma-Aldrich	Cat# L2020
ROCK inhibitor Y-27632	MilliporeSigma	Cat# SCM075
Laminin 511	BioLamina	Cat# LN511-0202
Fibronectin	Sigma-Aldrich	Cat# F4759
FluoroBrite™ DMEM	Gibco	Cat# A1896701
VECTASHIELD® HardSet™ Antifade Mounting Medium with DAPI	Vector Laboratories	Cat# H-1500-10

(*Continued on next page*)

Continued

REAGENT or RESOURCE	SOURCE	IDENTIFIER
Critical commercial assays		
Proteasome-Glo™ Chymotrypsin-Like Assay kit	Promega	Cat# G8621
RNeasy Mini kit	QIAGEN	Cat# 74104
Pierce™ BCA Protein Assay	Thermo Fisher Scientific	Cat# 23225
Deposited data		
Label-free proteomics (LFQ)	PRIDE	Accession: PXD056601
dSILAC proteomics (NIH/3T3)	PRIDE	Accession: PXD061384
dSILAC proteomics (mESCs)	PRIDE	Accession: PXD061306
RNA-seq	GEO	Accession: GSE278929
Analysis code and data processing scripts	GitHub	https://github.com/UPSUTER/ProTuCo
Experimental models: Cell lines		
NIH/3T3	Ueli Schibler, Geneva	N/A
HEK293T	ATCC	RRID:CVCL_0063
E14 mouse embryonic stem cells (mESCs)	Didier Trono, EPFL	N/A
CGR8 mouse embryonic stem cells (mESCs)	Sigma-Aldrich	Cat#07032901; RRID:CVCL_3987
H1 human embryonic stem cells (WA01, 46XY)	WiCell Research Institute	WA01
mESC SLT knock-in (ROSA26 locus, CGR8 background)	This study	N/A
hESC SLT knock-in (CLYBL locus, H1 background)	This study	N/A
hESC-derived neurons (iNGNs)	This study	N/A
hESC-derived astrocyte-enriched cultures	This study	N/A
Oligonucleotides		
Genotyping and integration-site PCR primers	This study	See Table S6
Recombinant DNA		
pDONOR MCS Rosa26	Addgene	Plasmid #37200
pCMV-RosaL6 ELD	Addgene	Plasmid #37198
pCMV-RosaR4 KKR	Addgene	Plasmid #37199
pC13N-dCas9-BFP-KRAB (CLYBL HDR)	Addgene	Plasmid #127968
pZT-C13-L1 (CLYBL left arm)	Addgene	Plasmid #62196
pZT-C13-R1 (CLYBL right arm)	Addgene	Plasmid #62197
pLV-pGK-rtTA3G-IRES-Bsd	PMID: 30146318	N/A
pLV-TRE3G-<gene of interest>	PMID: 30146318	N/A
PB_TRET_Ngn2-2A-Ngn1	Gift from Volker Busskamp	N/A
PB-transposase	Gift from Volker Busskamp	N/A
Software and algorithms		
MaxQuant (v1.6.10.43; v2.4.4.0)	PMID: 19029910	https://maxquant.org
Perseus (v1.6.12.0)	PMID: 29344888	N/A
STAR aligner (v2.7.x)	PMID: 23104886	N/A
DESeq2 (R 4.4.1)	PMID: 25516281	N/A
R (4.4.1)	R Core Team	N/A
TrackMate 7	PMID: 35654950	N/A
Cellpose 2.0	PMID: 36344832	N/A
scikit-learn	10.5555/1953048.2078195	N/A
Microfilm	https://github.com/guiwitz/microfilm	N/A
FastQC (v0.11.9)	Babraham Bioinformatics	N/A
FastQ Screen (v0.14.0)	Babraham Bioinformatics	N/A
bases2fastq (v1.8.0.1260801529)	Element Biosciences	N/A
Github code	This study	10.5281/zenodo.17283838

(*Continued on next page*)

Continued

REAGENT or RESOURCE	SOURCE	IDENTIFIER
Other		
Operetta CLS High-Content Imaging System	PerkinElmer	N/A
FACSAria cell sorter	BD Biosciences	N/A
4D-Nucleofector X Unit	Lonza	N/A
Amaxa P3 Primary Cell kit L	Lonza	Cat# V4XP-3012
96-well plate (black, clear bottom)	PerkinElmer	Cat# 6055302
Aviti Cloudbreak Freestyle flow cell	Element Biosciences	N/A
Dionex Ultimate 3000 RSLC nano UPLC	Thermo Fisher Scientific	N/A
Exploris Orbitrap 480 Mass Spectrometer	Thermo Fisher Scientific	N/A
Acclaim PepMap C18 precolumn	Thermo Fisher Scientific	N/A
ReproSil-Pur C18-AQ 1.9 μm beads	Dr. Maisch	N/A
Microcon-30K centrifugal filters	Merck	N/A
Tecan plate reader	Tecan	N/A

EXPERIMENTAL MODEL AND STUDY PARTICIPANT DETAILS

Cell Culture

NIH/3T3 and HEK293T cells were routinely cultured in DMEM (Gibco, 41966029), supplemented with 10% fetal bovine serum (Gibco, 10270-106), 1% penicillin/streptomycin (BioConcept, 401F00H) at 37°C, 5% CO_2. Cells were passaged by trypsinization (Sigma, T4049-100ML) every 2-3 days and maintained at a confluency < 80%.

E14 and CGR8 mouse embryonic stem cell lines were routinely cultured in GMEM (Sigma-Aldrich, G5154) supplemented with 10% ES cell-qualified fetal bovine serum (Gibco, 16141–079), 2 mM sodium pyruvate (Sigma-Aldrich, 113-24-6), 1% non-essential amino acids (Gibco, 11140–050), 1% penicillin/streptomycin (BioConcept, 4-01F00H), 2 mM L-glutamine (Gibco, 25030–024), 100 μM 2-mercaptoethanol (Sigma-Aldrich, 63689), leukaemia inhibitory factor (LIF — in-house), 3 μM GSK-3 Inhibitor XVI (Merck, 361559) and 0.8 μM PD184352 (Sigma-Aldrich, PZ0181), called hereafter 2i, at 37°C, 5% CO_2. Cells were plated on dishes coated with gelatin (Sigma-Aldrich, G9391). Cells were passaged every 2-3 days by trypsinization (Sigma-Aldrich, T4049) when density reached approximately 3.0×10^4 cells/cm^2 (Mulas et al. 2019).

H1 human embryonic stem cells (WiCell Research Institute, WA01, 46XY) were routinely cultured as colonies in mTeSR Plus (STEMCELL Technologies, 100-0276) with 0.2% penicillin/streptomycin (BioConcept, 401F00H) at 37°C, 5% CO_2. Cells were plated on dishes coated with Corning Matrigel hESC-qualified matrix (Corning, 354277). Cells were passaged every 4-7 days using the enzyme-free passaging reagent ReLeSR (STEMCELL Technologies, 05872), which preserves colonies, when most of the colonies were large with a dense center. For experiments requiring single-cell dissociation, i.e., nucleofection, sorting, and imaging, hESCs were passaged using Accutase (Innovative Cell Technology, AT104).

METHOD DETAILS

Production of lentiviral vectors and generation of stable cell lines

HEK293T cells were seeded at a density of 45,000 cells/cm^2 and transfected using calcium phosphate one day after seeding. Cells were co-transfected with PAX2 (envelope), MD2G (packaging), and the lentiviral construct of interest, and concentrated 120-fold by ultracentrifugation as described previously.[87] Target NIH/3T3 cells were seeded at a density of 13,000/cm^2 in a 24-well plate and transduced with 50 μL of concentrated lentivirus. For all dox-inducible cell lines, cells were first transduced with the pLV-pGK-rtTA3G-IRES-Bsd construct,[88] selected using 8 μg/mL of blasticidin (Thermofisher, A11139-03), transduced with the pLVTRE3G-construct of interest, and selected with puromycin (Thermofisher, A11138-03) at 2 μg/mL.

Generation of the mESC SLT knock-in cell line

The SLT construct under the control of the EF1α promoter was first inserted using InFusion cloning (Takara) into the pDONOR MCS Rosa26 plasmid (Addgene #37200) containing Rosa26 homology arms. CGR8 cells were co-transfected with pDONOR-SLT, pCMV-RosaL6 ELD (Addgene #37198), and pCMV-RosaR4 KKR (Addgene #37199) with the lipofectamine 3000 transfection reagent (Invitrogen, L3000001) in a 6-well plate following supplier instructions. These plasmids were a gift from Charles Gersbach.[53] Cells were then maintained for 2 weeks in culture. Cells were afterward sorted as single cells in 96-well plates for bright sfGFP and mOrange2 signals using a FACSAria (BD Biosciences) cell sorter. Around 1% of cells were positive. After 10 days of culture, single colonies were visually checked for MCFT fluorescence signal, and the brightest colonies were picked and amplified. 6 clones were then selected for characterization: gDNA was extracted using the DirectPCR Lysis Reagent (Viagen, 301-C) and PCRs were performed to verify the

correct integration site of the transgene[89] (Table S6). After gel validation, the bands were cut, the DNA amplicons were extracted with QIAquick Gel Extraction Kit (QIAgene, 28704), and sent to Sanger sequencing (Microsynth) to check the integration site for the presence of indels.

Generation of the hESC SLT knock-in cell line

The SLT construct was inserted using InFusion cloning (Takara) into the pC13N-dCas9-BFP-KRAB plasmid (Addgene, #127968), containing CLYBL homology arms and a CAG promoter. hESCs were co-transfected with pZT-C13-L1 (Addgene, #62196) and pZT-C13-R1 (Addgene, #62197) by nucleofection using the 4D-Nucleofector X Unit (Lonza) and Amaxa P3 Primary Cell kit L (Lonza, V4XP-3012), program CB-150. hESCs were supplemented with 1x CloneR2 (STEMCELL Technologies, 100-0691) supplement for the first two days. These plasmids were a gift from Jizhong Zou.[45] Cells were then maintained for 2 weeks in culture. Cells were afterward sorted as single cells in 96-well plates for bright sfGFP and mOrange2 signals using a FACS Aria (BD Biosciences) cell sorter. Around 0.4% of cells were positive. Cells were supplemented with 1x CloneR2 supplement for the first 4 days, with medium change every other day. After 14 days of culture, single colonies were visually checked for SLT signal, and the brightest colonies were picked and amplified. 3 clones were then selected for characterization: gDNA was extracted using the DNEasy Blood & Tissue kit (Qiagen, 69504) and PCRs were performed to verify the correct integration site of the transgene (Table S6). After running PCR products on an agarose gel, the bands were cut, the DNA amplicons were extracted using QIAquick Gel Extraction Kit (Qiagene, 28704), and verified by Sanger sequencing (Microsynth).

Generation of hESC-derived neurons (iNGNs)

hESCs were co-transfected with PB_TRET_Ngn2-2A-Ngn1 and PB-transposase plasmids by nucleofection as described earlier. These plasmids were a gift from Volker Busskamp.[90] After recovery, the cells were selected with puromycin (Thermofisher, A11138-03) at 3 μg/mL. hESCs were maintained as described earlier. hESCs were induced to neurons as described in [90] with slight modifications. Briefly, plates were coated with 15 μg/mL Poly-L-Ornithine (PLO, Sigma-Aldrich, P4957) and 10 μg/mL laminin (Sigma-Aldrich, L2020) in PBS. Plates were incubated for 2 h at room temperature after each coating step. 5 x 10^4 cells/cm^2 were plated as single cells on PLO/laminin-coated cultureware in mTeSR Plus medium (STEMCELL Technologies, 100-0276) supplemented with 10 μM ROCK inhibitor (MilliporeSigma, SCM075). For the next four days, the mTeSR Plus medium was supplemented with 1 μg/mL doxycycline (Sigma-Aldrich, D9891) and changed daily. On the last day, the medium was supplemented with 5 μM cytosine β-D-arabinofuranoside hydrochloride (Sigma-Aldrich, C6645). On day 5, neurons were passaged using Accutase (Innovative Cell Technology, AT104) and seeded 1.35 x 10^5 cells/well on a 96-well plate (Perkin Elmer, 6055302) coated with Corning Matrigel hESC-qualified matrix (Corning, 354277). After seeding, cells were cultured overnight in BrainPhys™ hPSC Neuron Kit (STEMCELL Technologies, 05795) supplemented with 200 nM ascorbic acid (STEMCELL Technologies, 72132) and 1 mM dibutyryl-cAMP (STEMCELL Technologies, 73882), using BrainPhys™ Imaging Optimized Medium (STEMCELL Technologies, 05796) as a basal medium. The next day, CHX treatment was performed for 48 h. The CHX concentration gradient was made of 56 different concentrations ranging from 0.002 to 5 μg/mL (Table S7).

Differentiation of hESCs into astrocytes

hESCs were first differentiated to neural progenitor cells using the STEMdiff SMADi Neural Induction kit (STEMCELL Technologies, 08581) according to the manufacturer's protocol for monolayer culture. Briefly, 2 x 10^5 cells/cm^2 were plated as single cells on Corning Matrigel hESC-qualified matrix (Corning, 354277) in STEMdiff Neural Induction Medium with SMADi supplement and 10 μM ROCK Inhibitor (Y-27632) (MilliporeSigma, SCM075). The next day, Y-27632 was removed, and the medium was changed daily. Cells were passaged three times every 7 days using Accutase (Innovative Cell Technology, AT104). One day after the third passage, the medium was changed to STEMdiff Astrocyte Differentiation Medium kit (STEMCELL Technologies, 100-0013) to obtain astrocyte precursors. The astrocyte precursors were maintained for three additional passages, changing the medium daily during the first week and every 2 – 3 days for the remaining weeks. Following three weeks of differentiation after the third passage of the precursors, the STEMdiff Astrocyte Maturation medium was used (STEMCELL Technologies, 100-0016). Maturation of astrocytes was performed for another three weeks, performing single cell passage every 7 days and medium change every 2 – 3 days, before the downstream analysis. N = 1 biological replicate.

Immunofluorescence for characterization of astrocyte-enriched cell culture

Astrocyte-enriched cultures were first fixed using 4 % formaldehyde (FA) (Thermo Fischer Scientific, 28906) in PBS that was added 1:1 to the culture medium and incubated for 5 min at room temperature (final FA: 2%). The medium was removed, and 4 % FA was added for 15 min at room temperature. After two washes with PBS, cells were permeabilized with 0.1 % Triton X-100 (BioChemica, UN3082) in PBS for 20 min and blocked with 1 % BSA (Sigma-Aldrich, A7906) in PBS for 30 min. Cells were incubated overnight at 4 °C with anti-Ki67 antibody (1:100, BD Biosciences, 550609) and anti-GFAP antibody (1:200, STEMCELL Technologies, 60048). The next day, cells were washed twice with PBS and incubated with an anti-mouse secondary antibody conjugated to AlexaFluor647 (1:1000, LifeTechnologies, A31571) for 1 h at room temperature. Cells were washed twice with PBS and mounted with VECTASHIELD® HardSet™ Antifade Mounting Medium with DAPI (Vector, H-1500-10). Imaging was performed with an Operetta CLS (Perkin Elmer) microscope, 20× objectives (Air immersion, Plan Apochromat, NA 0.8), at RT, using the following filters: Ex: BP 615-645, BP 650-675, Em: HC 655-760 for the antibody channels. N = 1 biological replicate.

Immunofluorescence for characterization of hESC-derived neurons (iNGN)

Immunofluorescence of hESC-derived neurons (iNGN) was performed as for astrocytes-enriched culture with minimal modifications. For fixation, we followed.[91] 0.1 M PHEM buffer (Electron Microscopy Sciences, 11162) was added 1:1 to the neuronal medium. Then, cells were washed twice with 0.1 M PHEM buffer (Electron Microscopy Sciences, 11162) before fixing with 4 % FA (Thermo Fisher Scientific, 28906), 0.25 % glutaraldehyde (Electron Microscopy Sciences, 16220) in 0.1 M PHEM buffer for 15 min at room temperature. After two washes with PBS, cells were permeabilized with 0.1 % Triton X-100 (BioChemica, UN3082) in PBS for 20 min and blocked with 1 % BSA (Sigma-Aldrich, A7906) in PBS for 30 min. Cells were incubated overnight at 4 °C with anti-Ki67 antibody (1:100, BD Biosciences, 550609), anti-MAP2 antibody (1:500, Sigma Aldrich AB5622), anti-TUBB antibody (1:2000, eBioscience 14-4510). The next day, cells were washed twice with PBS and incubated with an anti-mouse secondary antibody conjugated to AlexaFluor647 (1:1000, LifeTechnologies, A31571) or anti-rabbit secondary antibody conjugated to AlexaFluor647 (1:1000, LifeTechnologies, A21443) for 1 h at room temperature. Cells were washed twice with PBS and mounted with VECTASHIELD® HardSet™ Antifade Mounting Medium with DAPI (Vector, H-1500-10). Cells were imaged as described above. N = 1 biological replicate.

Immunofluorescence for characterization of pluripotency of mESC

4 days before imaging, mESCs were cultured in phenol-red-free N2B27 + 2i/LIF medium and seeded on a 96-well plate (Perkin Elmer, 6055302) coated with laminin 511 (BioLamina, LN511-0202). Before starting CHX treatment, mESCs were cultured for at least 2 weeks in N2B27 + 2i/LIF medium. The next day, CHX treatment was applied to each well following the designed concentration gradients: 0, 0.025, 0.05, 0.1, and 0.2 μg/mL, and cells were incubated for 72 h at 37 °C and 5% CO_2. After 72 h, the immunofluorescence of mESCs was performed as for astrocyte-enriched culture with minimal modifications. mESC were fixed using 4 % FA in PBS for 30 min at room temperature, cells were permeabilized with 0.5 % Triton X-100 (BioChemica, UN3082) in PBS for 20 min, and blocked with 1 % BSA (Sigma-Aldrich, A7906) in PBS for 30 min. Cells were incubated overnight at 4 °C with primary antibodies anti-SOX2 (1:500, Cell Signaling Technology 23064S), anti-NANOG (1:1000, Thermo Fisher MA5-31459), and anti-OCT4 (1:500, Cell Signaling Technology 5677). The next day, cells were washed twice with PBS and incubated with anti-rabbit secondary antibody conjugated to AlexaFluor647 (1:1000, LifeTechnologies, A21443) for 1 h at room temperature. After washing, VECTASHIELD® HardSet™ Antifade Mounting Medium with DAPI (Vector, H-1500-10) was added, and cells were imaged as described above. N = 1 biological replicate.

Snapshot imaging of the MCFT upon CHX/MYCi/INK128 steady-state treatments

3 days before imaging, NIH/3T3 cells were seeded on a 96-well plate (Perkin Elmer, 6055302) coated with fibronectin (Sigma, F4759) at a density that does not exceed 80% confluency for each well when imaging starts. After seeding, cells were cultured overnight without CHX in FluoroBrite™ DMEM medium (Gibco, A1896701) supplemented with 10% fetal bovine serum (Gibco, 10270-106), 2 mM L-glutamine (Gibco, 25030–024), and 1% penicillin/streptomycin (BioConcept, 401F00H). The next day, CHX treatment was applied to each well following the designed concentration gradients (Table S1). The CHX concentration gradient was made of 56 different concentrations ranging from 0.002 to 0.5 μg/mL. The medium containing the respective CHX concentrations was changed once after 24 hours. After 2 days of treatment, snapshot imaging was performed with Operetta CLS (Perkin Elmer), 20× objectives (Air immersion, Plan Apochromat, NA 0.8), at 37 °C, 5% CO_2. For the sfGFP channel, the following filters were used: Ex: BP 435-460, 460-490, Em: HC 500-550. For the mOrange2 channel, the following filters were used: Ex: BP 490-515, 530-560, Em: HC 570-650.

Experiments with H1 hESCs, astrocytes and CGR8 mESCs were performed similarly, except for culture conditions. hESCs were cultured in mTeSR1 without phenol red (STEMCELL Technologies, 05876) and seeded on a 96-well plate coated with Corning Matrigel hESC-qualified matrix (Corning, 354277). A 10 μM ROCK Inhibitor (Y-27632) (MilliporeSigma, SCM075) was added at the time of seeding. Mature astrocytes were seeded on a 96-well plate coated with Corning Matrigel hESC-qualified matrix (Corning, 354277) in Brain-Phys Without Phenol-Red (STEMCELL Technologies, 05791) supplemented with STEMdiff Astrocyte Maturation Supplement A and B (STEMCELL Technologies, 100-0037 and 100-0017).

mESCs were cultured in phenol-red free N2B27 + 2i/LIF medium and seeded on a 96-well plate coated with laminin 511 (BioLamina, LN511-0202). Before starting CHX treatment, mESCs were cultured for at least 2 weeks in N2B27 + 2i/LIF medium.

A similar protocol was used for anisomycin and MYCi treatments. The anisomycin concentration gradient was made of 56 different concentrations ranging from 0.0002 to 0.05 μg/mL (Table S2). The MYCi concentration gradient was made of 56 different concentrations ranging from 0.26 to 64 μM (Table S3).

For CHX treatment in combination with INK128, we proceeded as previously described, adding a constant concentration of INK128 to the CHX plate gradient. For hESCs, in each plate, wells whose cell number fell markedly below the expected dose–response trend were excluded as technical outliers attributable to under-seeding or uneven coating rather than true drug effects.

All experiments were performed with N = 2 biological replicates.

Snapshot imaging of the MCFT upon steady-state amino acids depletion

3 days before imaging, NIH/3T3 cells were seeded on a 96-well plate (Perkin Elmer, 6055302) coated with fibronectin (Sigma, F4759) at a density that does not exceed 80% confluency for each well when imaging starts. After seeding, cells were cultured overnight in FluoroBrite™ DMEM medium (Gibco, A1896701) supplemented with 10% fetal bovine serum (Gibco, 10270-106), 2 mM L-glutamine (Gibco, 25030–024), and 1% penicillin/streptomycin (BioConcept, 401F00H). The next day, medium was replaced by a mix between complete (with L-Arginine, L-Leucine, L-Lysine, L-Methionine) and amino acids-depleted DMEM medium (SILAC DMEM High

Glucose (Athena, 0430), 3.7 g/L Sodium Bicarbonate, 0.2 mM Sodium Pyruvate (Sigma-Aldrich, S8636), 10% fetal bovine serum (Gibco, 10270-106), 2 mM L-glutamine (Gibco, 25030–024, 1% penicillin/streptomycin (BioConcept, 401F00H)). The proportions of the mix are given in Tables S4A and S4B. The cells were kept for 2 days in culture before imaging. Snapshot imaging was performed with Operetta CLS (Perkin Elmer), 20× objectives (Air immersion, Plan Apochromat, NA 0.8), at 37 °C, 5% CO_2. For the sfGFP channel, the following filters were used: Ex: BP 435-460, 460-490, Em: HC 500-550. For the mOrange2 channel, the following filters were used: Ex: BP 490-515, 530-560, Em: HC 570-650. N = 2 biological replicates.

Live imaging of the MCFT upon CHX treatment/release

3 days before imaging, NIH/3T3 cells were seeded on a 96-well plate coated with fibronectin (Sigma, F4759) at a density that does not exceed 80% confluency for each well when imaging starts. Four conditions were designed: control (-CHX), CHX (2 days of treatment with 0.1 μg/ml CHX before imaging), pulse (0.1 μg/ml CHX added right before imaging), and release (2 days of treatment with 0.1 μg/ml CHX before imaging, followed by CHX removal immediately before imaging). 500 cells were seeded per well for control and pulse conditions. 1000 cells were seeded per well for CHX and release conditions. After seeding, cells were cultured overnight without CHX in FluoroBrite™ DMEM (Gibco, A1896701) supplemented with 10% fetal bovine serum (Gibco, 10270–106), 2 mM L-glutamine (Gibco, 25030–024), and 1% penicillin/streptomycin (BioConcept, 401F00H). The next day, CHX was applied at 0.1 μg/ml in CHX and release conditions. During the treatment, the medium was changed every 24h. Before imaging, all wells were washed once with medium. Then, medium containing 0.1 μg/ml CHX was added to CHX and pulse conditions. In control and release conditions, medium without CHX was added. Live imaging was performed with Operetta CLS (Perkin Elmer), 20× objectives (Air immersion, Plan Apochromat, NA 0.8), at 37 °C, 5% CO_2, with 15 min intervals for more than 20 h if not specified otherwise. For the sfGFP channel, the following filters were used: Ex: BP 435-460, 460-490, Em: HC 500-550. For the mOrange2 channel, the following filters were used: Ex: BP 490-515, 530-560, Em: HC 570-650.

Experiments with H1 hESCs, human astrocytes, and CGR8 mESCs were performed similarly, except for the culture conditions that were as described in the previous section.

For the CHX pulse experiment in the presence of 25 nM INK128 or 200 nM ISRIB, we proceeded as previously described, pre-treating the cells for 1 h with the respective drugs before adding the medium with CHX, keeping the INK128/ISRIB concentration constant.

All time-lapse experiments were performed at least in N = 2 biological replicates, except for human astrocytes (N = 1 biological replicate).

Live imaging of the MCFT upon MYCi treatment/release

3 days before imaging, NIH/3T3 cells were seeded on a 96-well plate coated with fibronectin (Sigma, F4759) at a density that does not exceed 80% confluency for each well when imaging starts. Four conditions were designed: control (-MYCi), MYCi (2 days of treatment with 64 μM MYCi before imaging), pulse (64 μM MYCi added right before imaging), and release (2 days of treatment with 64 μM MYCi before imaging followed by MYCi removal immediately before imaging). 254 cells were seeded per well for control and pulse conditions. 800 cells were seeded per well for MYCi and release conditions. After seeding, cells were cultured overnight without MYCi in FluoroBrite™ DMEM (Gibco, A1896701) supplemented with 10% fetal bovine serum (Gibco, 10270-106), 2 mM L-glutamine (Gibco, 25030–024), and 1% penicillin/streptomycin (BioConcept, 401F00H). The next day, MYCi was applied at 64 μM in MYCi and release conditions. During the treatment, the medium was changed every 24h. Before imaging, all wells were washed once with medium. Then, medium containing 64 μM MYCi was added to MYCi and pulse conditions. In control and release conditions, medium without MYCi was added. Live imaging was performed with Operetta CLS (Perkin Elmer), 20× objectives (Air immersion, Plan Apochromat, NA 0.8), at 37 °C, 5% CO_2, with 15 min intervals for more than 20 h if not specified otherwise. For the sfGFP channel, the following filters were used: Ex: BP 435-460, 460-490, Em: HC 500-550. For the mOrange2 channel, the following filters were used: Ex: BP 490-515, 530-560, Em: HC 570-650.

All time-lapse experiments were performed at least in N = 2 biological replicates.

SNAP-tag pulse-chase labeling

Cells were seeded and cultured in 96-well plates following the previous live imaging method section. 45 minutes before imaging, cells were incubated with an imaging medium that contained 40 - 80 nM SNAP Cell 647 Sir dye (NEB, S9102S) for 30 min at 37°C, 5% CO_2. Cells were then gently washed five times with fresh medium. The medium was then replaced with a fresh imaging medium containing 1 μM SNAP Cell Block (NEB, S9106S) to prevent the binding of residual SNAP dye to newly synthesized SNAP-tagged proteins. Imaging was performed with an Operetta CLS (Perkin Elmer) microscope, 20× objectives (Air immersion, Plan Apochromat, NA 0.8), at 37 °C 5% CO_2, at 15 min intervals. For the sfGFP channel, the following filters were used: Ex: BP 435-460, 460-490, Em: HC 500-550. For the SNAP channel, the following filters were used: Ex: BP 615-645, BP 650-675, Em: HC 655-760.

All time-lapse experiments were performed at least in N = 2 biological replicates.

Dox pulse-chase experiment

Three days before imaging, NIH/3T3 cells were seeded at a density of 200 cells/well on a 96-well plate coated with fibronectin (Sigma, F4759). After seeding, cells were cultured overnight without dox in FluoroBrite™ DMEM (Gibco, A1896701) supplemented with 10% fetal bovine serum (Gibco, 10270-106), 2 mM L-glutamine (Gibco, 25030–024), and 1% penicillin/streptomycin (BioConcept, 401F00H). The next day, dox (Sigma-Aldrich, D9891) treatments were applied at the desired concentrations. During the treatment,

the medium was changed every 24 hours. Before imaging, all wells were washed three times with warm PBS followed by the addition of medium containing the desired dox concentration. Live imaging was performed thereafter (~15min delay) with an Operetta CLS (Perkin Elmer), 20× objectives (Air immersion, Plan Apochromat, NA 0.8), at 37 °C, 5% CO_2, with 15 min intervals for at least 20 h if not specified otherwise. For the sfGFP channel, the following filters were used: Ex: BP 435-460, 460-490, Em: HC 500-550. For the mOrange2 channel, the following filters were used: Ex: BP 490-515, 530-560, Em: HC 570-650.

This experiment was performed with N = 1 biological replicate.

Flow cytometry

Cells were trypsinized, resuspended in culture medium with 50 mM Hoechst33342 (Thermo Fisher Scientific #H3570), and incubated for 15 min at 37°C. Cells were then spun down, resuspended in cold PBS with 2% FBS, and analyzed by flow cytometry on a LSR Fortessa. One experimental replicate was performed for each cell line and each CHX concentration, and at least 10,000 cells per sample were analyzed.

Imbalance computation

The imbalance θ, introduced in[50] is defined as:

$$\theta(t) = \frac{k(t) \times P(t)}{s(t)}$$

The protein synthesis and decay rates at time t, $s(t)$, and $k(t)$ respectively, were inferred using the Hierarchical Bayesian inference algorithm introduced hereafter (see also supplemental text for details). The total protein level at time t, $P(t)$, was calculated by summing up the measured green G signal and the inferred black-green B_G signal such that:

$$P(t) = G_{measured}(t) + B_{G,infered}(t)$$

N-Hydroxysuccinimide (NHS ester) labeling and imaging

Cells were seeded in a 96-well plate coated with fibronectin (Sigma, F4759) and cultured overnight. The cell seeding number was adjusted so that none of the wells would be more than 80% confluent on day 7. On day 2, 48 different CHX concentrations ranging from 0.002 to 0.25 μg/mL were applied to cells for the next 6 days. The medium was changed every 48 hours. On day 7, cells were fixed with 4% formaldehyde in PBS for 15 min at RT before washing once with PBS. Then, cells were permeabilized with 100% pre-cooled methanol at -20°C for 10 min. Before staining, cells were washed once with 0.2 M sodium bicarbonate. N-Hydroxysuccinimide (Invitrogen, A37573) was diluted in 0.2 M sodium bicarbonate to a final concentration of 50 μg/mL and applied to cells at RT for 30 min. Cells were washed twice with PBS and mounted with Vectashield containing DAPI (Vector, H-1500-10). Imaging was performed with an Operetta CLS (Perkin Elmer) microscope, 20× objectives (Air immersion, Plan Apochromat, NA 0.8), at RT, using the following filters: Ex: BP 615-645, BP 650-675, Em: HC 655-760 for the NHS-ester channel.

For iNGNs, cells were plated in 96-well plates as described previously. After 48 h of treatment with the desired drug concentrations (Table S7), the cells were fixed as described in the immunofluorescence protocol, and the experimental procedure for NHS-ester labeling was followed.

NHS-ester experiments were performed in N = 2 biological replicates.

HPG labelling in iNGNs

The assay was performed using the Click-iT® HPG Alexa Fluor® Protein Synthesis Assay Kit (C10428) according to the supplier's instructions. Cells were plated in 96-well plates as described previously. After treatment of the cells with the desired drug concentrations, cells were incubated with methionine-free SILAC - Neural Basal Medium (AthenaES, 0428) supplemented as neuronal medium described above, as well as 50 μM Click-iT® HPG (Invitrogen, C10186), missing amino-acids and the corresponding concentration of CHX, for 30 min at 37°C, 5% CO2. Negative control cells were treated with CHX 200 μg/ml for 30 min prior incubation in methionine-free medium. Cells were fixed as described earlier. Then, cells were washed twice with 3% BSA in PBS. Permeabilization was performed by incubation of the cells with 0.5% Triton X-100 in PBS for 20 min at room temperature. The Click reaction was then performed by strictly following the supplier protocol, replacing the Alexa Fluor® 488 azide with Alexa Fluor® 647 azide (A10277). After the last rinse step, cells were mounted using VECTASHIELD® HardSet™ Antifade Mounting Medium with DAPI (H-1500-10).

This experiment was performed in N = 1 biological replicate.

ELISA for p70S6K

To measure phosphorylation levels of p70 S6K in NIH/3T3 and mES cells, we used the Multispecies p70 S6 Kinase (Total/Phospho) InstantOne™ ELISA Kit (Invitrogen). We followed the manufacturer's assay protocol for adherent cells. Briefly, we plated 5,000 to 10,000 (48 h timepoint) cells per well of a 96-well plate and treated the cells with 0.1 μg/mL CHX for different durations (0, 1, 2, 5 and 48 hours). After 48 hours, we performed cell lysis using 150 μL per well of the Cell Lysis Buffer Mix (1X) supplemented with benzonase. We then proceeded as described by the manufacturer.

This experiment was performed in N = 3 biological replicates.

Proteasome-Glo assay

Cells were plated in 96-well plates and treated as described in the corresponding figure. The assay for the detection of the proteasome activity (Chymotrypsin-like activity) was performed using the Proteasome-Glo™ Chymotrypsin-Like Assay kit, following supplier's recommendations (Promega, G8621). Briefly, cells were lysed in 35 μL/well of 50 mM Tris pH 8 with 0.1% NP-40. 25 μL of the protein extracts were incubated with 25 μL of Proteasome-Glo™ Reagent in a new white 96-well plate. The content of the plate was then gently mixed using a plate shaker at 400 rpm for 30 seconds before incubation at room temperature for 15 min. The luminescence signal was recorded on a Tecan plate reader. In parallel, 5 μL of the protein extract was used to perform a Pierce™ BCA assay (Thermo Fisher Scientific).

This experiment was performed in N = 3 biological replicates.

RNA-seq

Sample collection

The experiment was performed with N = 4 biological replicates. NIH/3T3 and mES cells were cultured in the standard conditions described above. At timepoint 0 h, CHX at a final concentration of 0.1μg/mL was pulsed into the medium. At subsequent timepoints (1 h, 2 h, 5 h, 48 h), cells were washed once in PBS and directly lysed using the lysis buffer of the RNeasy Mini kit (Quiagen). RNA extraction was then performed according to the manufacturer's instructions. RNA quality and concentration were assessed using Nanodrop and TapeStation 4200 (Agilent), which confirmed their integrity.

Sample preparation and sequencing

Libraries for mRNA-seq were prepared with the Stranded mRNA Ligation method (Illumina), according to manufacturer's instructions, starting from 300ng RNA. Libraries, all bearing unique dual indexes, were subsequently loaded at 9.9 pM on an Aviti Cloudbreak Freestyle flow cell (Element Biosciences) and sequenced according to manufacturer instructions, yielding pairs of 80 nucleotides reads at a depth of about 30 mio reads pairs per sample. Reads were trimmed of their adapters with bases2fastq version 1.8.0.1260801529 (Element Biosciences) and quality-controlled with fastQC v0.11.9. FastQ Screen v0.14.0 tool was used for screening FASTQ files reads against multiple reference genomes.

Data analysis

Indexes were generated with STAR[92] using GRCm39 mouse genome assembly with option –sjdbOverhang 100. The reads were then aligned using STAR using the –quantMode GeneCounts option. A count matrix was then generated using an in-house Python script that takes as input the ReadsPerGene.out.tab files generated by STAR alignment. DESeq2[93] was then used in R 4.4.1[94] in order to perform differential expression analysis. The output was then analyzed in Python using standard libraries. Lists of ribosomal and mitochondrial genes were respectively taken from.[95,96]

Label-free Mass Spectrometry experiments

Sample collection

The experiment was performed in N = 4 biological replicates. In each condition (DMSO or 0.1 μg/mL CHX), one 10 cm culture dish at <80% confluency was used. Cells were washed twice in PBS without Mg^{2+} and Ca^{2+} (PBS -/- hereafter), trypsinized, collected in a 15 mL tube, and pelleted by centrifugation at 300g for 5 min. The supernatant was then discarded, and the cell pellet was snap-frozen in liquid nitrogen. Once all samples were collected, the pellets were resuspended in lysis buffer (100 mM Tris buffer pH 8, 2% SDS, 1X Halt™ Protease Inhibitor, and 1:50 v:v Benzonase nuclease) and incubated 15 min at room temperature. The samples were then boiled at 90°C for 10 min and centrifuged at 16'000g for 10 min at 4°C. The supernatant was then transferred to a new tube and the protein extract concentration was measured using a Pierce™ BCA assay (Thermo Fisher Scientific).

Sample preparation for Mass Spectrometry

Mass spectrometry-based proteomics-related experiments were performed by the Proteomics Core Facility at EPFL. Each sample was digested by filter-aided sample preparation (FASP)[97] with minor modifications. Proteins (20 μg) were deposited on top of washed and conditioned Microcon®-30K devices (Merck AG, Zug, Switzerland). Samples were centrifuged at 9400×*g*, at 20°C for 30 min. or until complete dryness. All subsequent centrifugation steps were performed using the same conditions. Two washing steps were performed using 200 μL urea solution (8 M Urea, 100 mM Tris-HCl pH 8). Reduction was performed by adding 100 μL of 10 mM Tris(2-carboxy)phosphine (TCEP) in urea solution on top of filters, followed by 60 min incubation time at 37°C with gentle shaking and light protection. The reduction solution was removed by centrifugation and two washing steps with 200 μL urea solution. Then, alkylation was performed by adding 100 μL of 40 mM chloroacetamide (CAA) in urea solution and incubating the filters at 37°C for 45 min with gentle shaking and protection from light. The alkylation solution was removed by centrifugation, followed by two washing steps with 200 μL of urea solution. Finally, two additional washing steps using 200 μL of 5 mM Tris-HCl pH 8 were performed to condition the filters for digestion. Proteolytic digestion was performed overnight at 37°C by adding 100 μL of a combined solution of Endoproteinase Lys-C and Trypsin Gold in an enzyme/protein ratio of 1:50 (w/w) prepared in 5 mM Tris-HCl and 10 mM $CaCl_2$ on top of filters. The resulting peptides were recovered by centrifugation and two subsequent elutions with 50 μL of 4% trifluoroacetic acid. Finally, the recovered peptides were desalted on SDB-RPS StageTips[98] and dried by vacuum centrifugation prior to LC-MS/MS injections.

Mass spectrometry

Samples were resuspended in 2% acetonitrile (Biosolve), 0.1% FA and nano-flow separations were performed on a Dionex Ultimate 3000 RSLC nano UPLC system (Thermo Fischer Scientific) on-line connected with an Exploris Orbitrap 480 Mass Spectrometer

(Thermo Fischer Scientific). A capillary precolumn (Acclaim Pepmap C18, 3 μm-100Å, 2 cm x 75μm ID) was used for sample trapping and cleaning. A 50 cm long capillary column (75 μm ID; in-house packed using ReproSil-Pur C18-AQ 1.9 μm silica beads; Dr. Maisch) was then used for analytical separations at 250 nl/min over 150 min biphasic gradients. Acquisitions were performed through Top Speed Data-Dependent acquisition mode using a cycle time of 2 seconds. First MS scans were acquired with a resolution of 60'000 (at 200 m/z) and the most intense parent ions were selected and fragmented by High energy Collision Dissociation (HCD) with a Normalized Collision Energy (NCE) of 30% using an isolation window of 1.4 m/z. Fragmented ions were acquired with a resolution of 15'000 (at 200m/z) and selected ions were then excluded for the following 20 s.

Data analysis

Raw data were processed using MaxQuant 1.6.10.43[99] against 55286 entries (LR2022_05), Carbamidomethylation was set as fixed modification, whereas oxidation (M), phosphorylation (S, T, Y), acetylation (Protein N-term), and glutamine to pyroglutamate were considered as variable modifications. A maximum of two missed cleavages was allowed, and the "Match between runs" option was enabled. A minimum of 2 peptides was required for protein identification, and the false discovery rate (FDR) cutoff was set to 0.01 for both peptides and proteins. Label-free quantification and normalization were performed by MaxQuant using the MaxLFQ algorithm, with the standard settings.[100] Statistical analysis was performed using Perseus version 1.6.12.0[101] from the MaxQuant tool suite. Reverse proteins, potential contaminants, and proteins only identified by sites were filtered out. Protein groups containing at least 3 valid values in at least one condition were conserved for further analysis. Empty values were imputed with random numbers from a normal distribution (Width: 0.4 and Down shift: 1.8 std). A two-sample t-test with permutation-based FDR statistics (250 permutations, FDR = 0.01, S0 = 1) was performed to determine significantly differentially abundant candidates. Lists of ribosomal and mitochondrial proteins were respectively taken from Tweedie et al..[95] and Rath et al.[96]

Dynamic SILAC

Cell culture

NIH/3T3 cells were cultured at least 2 weeks in light medium: DMEM for SILAC (Thermo scientific) supplemented with PS, dialyzed FBS (Thermo scientific), (light) L-Lysine-2HCl (0.666 mM), (light) L-Arginine-HCl (0.399 mM),[44] and L-Proline (200 mg/L).[102] mESCs were cultured at least 2 weeks in medium-heavy medium: N2B27 for SILAC (DMEM/F12 for SILAC (AthenaES), Neurobasal for SILAC (AthenaES), Sodium Pyruvate (40 mg/mL), N2 (1X), B27 (0.5X), Pen/Strep (1%), L-glutamine (2 mM), beta-mercaptoethanol (50 μM)) + 2i/LIF supplemented with (medium-heavy) $^{13}C_6$ $^{15}N_4$ L-arginine (0.65 mM), (medium-heavy) $^{13}C_6$ L-arginine (0.55 mM), and L-Proline (200 mg/L).[102] Before switching from light (NIH/3T3) or medium-heavy (mESC) to heavy medium, cells were treated with 0.05 μg/mL CHX or equivalent dilution of DMSO in 6-well plates. Note that we decided to treat the cells with 0.05 μg/mL CHX instead of the usual 0.1 μg/mL concentration due to the lower division rate of NIH/3T3 in the SILAC medium. At timepoint 0 h, we replaced light or medium-heavy medium with pre-warmed heavy medium: DMEM for SILAC (Thermo scientific) supplemented with PS, dialyzed FBS (Thermo scientific), (heavy) $^{13}C_6$ $^{15}N_2$ L-Lysine-2HCl (0.666 mM), (heavy) $^{13}C_6$ $^{15}N_4$ L-Arginine-HCl (0.399 mM), and L-Proline (200 mg/L) for NIH/3T3; N2B27 for SILAC (Thermo scientific) supplemented with (heavy) $^{13}C_6$ $^{15}N_2$ L-Lysine-2HCl (0.65 mM), (heavy) $^{13}C_6$ $^{15}N_4$ L-Arginine-HCl (0.55 mM), and L-Proline (200 mg/L) for mESC.

Sample collection

At the corresponding timepoint, the culture dish was placed on ice, the medium aspirated, and the cells washed twice with ice-cold PBS without Mg^{2+} and Ca^{2+} (PBS -/- hereafter). Cells were then scraped in 50 μL of lysis buffer (100 mM Tris buffer pH 8, 2% SDS, 1X Halt™ Protease Inhibitor, and 1:50 v:v Benzonase nuclease), collected in a 1.5 mL Eppendorf *protein LoBind* tube, and incubated for 15 min at room temperature. The protein extract was then snap-frozen in liquid nitrogen. Once all samples were collected, the samples were boiled at 90°C for 10 min and centrifuged at 16'000 x g for 10 min at 4°C. The supernatant was then transferred to a new tube, and the protein extract concentration was measured using a BCA assay (Pierce).

Sample preparation for Mass Spectrometry

Protein samples were prepared as described above for the Label-free Mass Spectrometry experiments. One replicate was performed for each condition (DMSO or CHX) and time point.

Mass spectrometry

Samples were resuspended as defined earlier, but the separation was performed using a Vanquish Neo nano UPLC system (Thermo Fischer Scientific), on-line connected with an Orbitrap Fusion Lumos Tribrid Mass Spectrometer (Thermo Fischer Scientific). The same parameters were used for the separation on the gradient, but the ones of the MS acquisition were slightly different. Acquisitions were performed through Top Speed Data-Dependent acquisition mode using a cycle time of 1 second. First MS scans were acquired with a resolution of 240K (at 200 m/z) on the orbitrap, and the most intense parent ions were selected and fragmented by High energy Collision Dissociation (HCD) with a Normalized Collision Energy (NCE) of 30% using an isolation window of 0.7 m/z. Fragmented ions were acquired on the ion trap with a maximum injection of 20 ms, and selected ions were then excluded for the following 20 s.

Data analysis

Raw data were processed using MaxQuant 2.4.4.0[99] against 54822 entries (LR2024_01) using the parameters taken from[70] with slight modifications as described in Tables a and b below:

Table a. MaxQuant parameters used for dSILAC in NIH/3T3 cells

Category	Parameter	A: Turnover analysis (dynamic SILAC)	B: (Re-)incorporation of light amino acids	C: LFQ analysis of t=0 samples
Group specific parameters				
Type	Type	Standard	Standard	Standard
	Multiplicity	2	1	1
	Max labeled AAs	3	-	-
	Labels	Light: Heavy: Arg10, Lys8	-	-
Modifications	Variable	Oxidation (M) Acetyl (N-term Protein)	Oxidation (M) Acetyl (N-term Protein) Arg10 as PTM Lys8 as PTM	Oxidation (M) Acetyl (N-term Protein) Gln -> pyro-Glu Phospho (STY)
	Fixed	Carbamidomethyl (C)	Carbamidomethyl (C)	Carbamidomethyl (C)
	Max nb of modif.	5	5	5
Label-free quantification	LFQ	None	None	LFQ
	LFQ min. ratio count	-	-	2
	Normalisation type	-	-	Classic
Misc.	Requantify	FALSE	FALSE	FALSE
Digestion	Digestion mode	Specific	Specific	Specific
	Enzyme	Trypsin	Trypsin	Trypsin
	Max. missed cleavages	2	2	2
Global parameters				
Sequences	Fasta files	Uniprot_Mouse _54822Sequences_LR2024_01		
	Include contaminants	TRUE	TRUE	TRUE
Protein quantification	Label min. ratio count	2	1	2
	Peptides for quantification	Unique + razor	All	Unique + razor
Identification	Min. peptides	2	1	2
	Min. Razor + unique peptides	2	1	2
	Min. unique peptides	1	0	1
	Match between runs	TRUE	TRUE	TRUE

Table b. MaxQuant parameters used for dSILAC in mESC

Category	Parameter	A: Turnover analysis (dynamic SILAC)	B: (Re-)incorporation of light amino acids	C: LFQ analysis of t=0 samples
Group specific parameters				
Type	Type	Standard	Standard	Standard
	Multiplicity	2	1	1
	Max labeled AAs	3	-	-
	Labels	Light: Arg6, Lys4 Heavy: Arg10, Lys8	-	Arg6 Lys4
Modifications	Variable	Oxidation (M) Acetyl (N-term Protein)	Oxidation (M) Acetyl (N-term Protein) Arg6 as PTM Arg10 as PTM Lys4 as PTM Lys8 as PTM	Oxidation (M) Acetyl (N-term Protein) Gln -> pyro-Glu Phospho (STY)
	Fixed	Carbamidomethyl (C)	Carbamidomethyl (C)	Carbamidomethyl (C)

(*Continued on next page*)

Table b. ***Continued***

Category	Parameter	A: Turnover analysis (dynamic SILAC)	B: (Re-)incorporation of light amino acids	C: LFQ analysis of t=0 samples
	Max nb of modif.	5	5	5
Label-free quantification	LFQ	None	None	LFQ
	LFQ min. ratio count	-	-	2
	Normalisation type	-	-	Classic
Misc.	Requantify	FALSE	FALSE	FALSE
Digestion	Digestion mode	Specific	Specific	Specific
	Enzyme	Trypsin	Trypsin	Trypsin
	Max. missed cleavages	2	2	2
Global parameters				
Sequences	Fasta files	Uniprot_Mouse _54822Sequences_LR2024_01		
	Include contaminants	TRUE	TRUE	TRUE
Protein quantification	Label min. ratio count	2	1	2
	Peptides for quantification	Unique + razor	All	Unique + razor
Identification	Min. peptides	2	1	2
	Min. Razor + unique peptides	2	1	2
	Min. unique peptides	1	0	1
	Match between runs	TRUE	TRUE	TRUE

Computation of protein half-life

Rates were computed with N = 1 biological replicate for the entire dynamic SILAC experiment. We provide a detailed description of the analysis steps in the supplemental text and the scripts deposited on GitHub. Briefly, we followed[70] by first filtering out contaminants, decoy sequences, and peptides exhibiting a false heavy signal in the unlabeled control sample. We then computed the percentage of old (light) peptides *%old* according to:

$$\%old = 1 - \frac{1 - \%L}{P(H)^{MC+1}}$$

In which *%L* is the fraction of remaining light peptide, *P(H)* is the probability of heavy Lys/Arg incorporation, and *MC* is the number of missed cleavages. Considering *P(H)*, we correct for light amino acid recycling. In the experiment presented in the main text for NIH/3T3, we assumed $P(H) \sim 1$ since the measured $P(H)=0.985$. For mESC, $P(H) = 0.95$. Grouping peptides per protein group, we then performed a linear fit according to the following equation:

$$\ln(\%old) = -k \times t$$

In which k is the decay rate and t is the incubation time in the heavy medium. We kept protein groups for which $r^2 > 0.9$ following.[44] Finally, we computed the protein half-life using the following equation:

$$t_{1/2} = \frac{\ln(2)}{k}$$

Image pre-processing

For background correction, image intensity was modeled in the following way:

$$I_{total} = f \times (I_{FOI} + I_{AF} + D)$$

I_{total} is the intensity value of the raw image. f is the uneven illumination pattern. I_{FOI} is the fluorescence signal of interest. I_{AF} is the auto-fluorescence from the medium. D is the dark field signal. D was ignored as it was negligible compared to I_{FOI} or I_{AF}. f was generated by imaging a well with medium only using the same exposure settings. This image was subsequently normalized to its mean pixel intensity. Raw images were divided by the image from the well with medium only to generate flat-field corrected images. I_{AF} was calculated for every single frame by applying the appropriate thresholding method to the field-corrected images, which created a binary image that masked foreground signals I_{FOI}. The threshold was determined using the fifth percentile of the intensity distribution of the pixels belonging to segmented cells. The mask was then enlarged by erosion. Finally, the mean or the peak of pixel intensities was measured from the unmasked region. We did not generate background-subtracted images but rather subtracted this value from final single-cell measurements inside a Jupyter notebook.

Cell segmentation and tracking

For segmentation and tracking nuclear fluorescent signals, Trackmate (7.1)[103] was used through a groovy script (written by Olivier Burri and Romain Guiet, EPFL) that enables image processing in batch. This script was tailored for using Stardist[104] as the detector to segment cell nuclei on the sfGFP channel. Tracking was then performed with the LAP algorithm[105] within the same script. The script generated Trackmate XML files that allow for reviewing the tracking result with the Trackmate user interface. Both sfGFP and mOrange2 traces were smoothed with a Savitzky-Golay filter (window length: 100, polynomial order: 6)[106] before superstatistical modeling. For the CHX pulse and release experiment in hESCs and mESCs, fluorescence trajectories were detrended using the Control and the +CHX conditions, respectively. For the NHS-ester labeling and mESC/hESC experiments, CellPose in Python[107] was used to segment the nuclei. The masks were then used to retrieve NHS-ester SiR-647 nm integrated intensities of individual cells. All microscopy figure panels and supplemental videos were made using the microfilm package[108] in Python.

Quantification of k and k_{deg} from SNAP pulse-chase labeling

To measure k_{deg} with SNAP, the integrated intensity for each single cell trajectory or single lineage (mother and computationally-fused daughter cells) trajectory was transformed by natural logarithm, then linear-fitted a robust RANSAC[109] regression (random state: 42) from the scikit-learn package 1.0.2.[110] Fluorescence intensities of daughter cells resulting from cell division were summed. To measure the total protein decay rate k with SNAP ($k_{deg} + k_{dil}$), the mean intensities for each lineage were transformed by natural logarithm and then linearly fitted with a robust regressor RANSAC (random state: 42). Fluorescence intensities of daughter cells resulting from cell division were averaged.

Quantification of S and k from the MCFT

The decay rate k was computed using the formula derived in the supplemental text. The procedure to calibrate the MCFT is given in the supplemental text. To compute the rates s, we assumed equilibrium for all our measurements. With μ_G, μ_R, the integrated intensity for sfGFP and mOrange2 fluorescence, and m_G the maturation rate of sfGFP (Figure1A), we computed the synthesis rate as:

$$s = \mu_G \times \frac{k(m_G+k)}{m_G}$$

s is thus given here in relative units (fluorescence/hour). In the main text, we use S when s is normalized to the control condition, such that for control conditions we have $S=1$. See supplemental text for details. To compute $s_{conc.}$ we used the same equation, replacing the integrated intensity μ_G with the mean intensity $\widehat{\mu_G}$ (average fluorescence intensity per pixel). The equation linking the two observables is:

$$\widehat{\mu_G} = \frac{\mu_G}{\#pixels}$$

In the main text, we use $S_{conc.}$ when $s_{conc.}$ is normalized to the median synthesis rate in a cell line (Figure 5).

Quantification of k_{dil} from time-lapse movies

To measure k_{dil}, we counted cell numbers per imaging frame over time. The dilution rate was then calculated by log2 transformation of the cell number and linear fitting with the RANSAC regressor (random state: 42).

Modeling and inference from MCFT traces

We adopted a superstatistical Bayesian inference algorithm,[47–49] designed for autoregressive models (AR-1), and applied it to our ordinary differential equation (ODE) systems. Briefly, we computed the (joint) posterior distribution of S and k along with the latent variable B_G at each timepoint and propagated this posterior forward and backward along the MCFT trajectories. In our case, the trajectories used for the inference are G (sfGFP) and R (mOrange2) fluorescence trajectories acquired by live-cell imaging. Propagation of the posterior distribution relies on two hyperparameters chosen for their ability to recapitulate the data (data retrodiction) and fixed for a whole dataset. Details are given in the supplemental text and in Figures S8–S12.

Modeling and inference from SNAP trajectories

We adopted a superstatistical Bayesian inference algorithm,[47–49] designed for autoregressive models (AR-1), and applied it to an exponential decay model with a variable rate. Briefly, we computed the posterior distribution of k at each timepoint and propagated this posterior forward and backward along the SNAP trajectory. The SNAP trajectory was assembled by combining SNAP trajectories obtained through SNAP pulse-chase experiments at different time points after CHX release. The combination was done by aligning the trajectories in time. Each trajectory was normalized to the data point value of the previous trajectory (or 1 for the first) at its initial time point, and an average was calculated for each overlapping time point of the remaining segments of the trajectories. Propagation of the posterior distribution relies on two hyperparameters chosen for their ability to recapitulate the data (data retrodiction) and fixed for a whole dataset. Details are given in the supplemental text.

Log-likelihood and bootstrapping for model selection

Log-likelihood was computed using a Gaussian error model. The pseudo-(log) likelihood was used for the actual computation, finally reducing to the residual sum of squares. Briefly, data were compared to the model predictions for the passive adaptation, no-adaptation, and perfect adaptation models. To compute statistics for the log-likelihood estimator, bootstrapping was performed with N = 1000 resampling, keeping the sample size constant.

QUANTIFICATION AND STATISTICAL ANALYSIS

Statistical analysis was performed using Python and the scipy.stats package. All details about statistical tests and sample size are available in the figures' legends. $p < 0.05$ was considered statistically significant. When Pearson correlation was performed, the statistics (p-value and determination coefficient r^2) were computed and displayed on the figure or specified in the figure legend. Data binning was performed using an in-house algorithm. Briefly, the number of bins was fixed over the full range of values of the x-axis. For each bin, we then computed the median of the y-values of all data points belonging to it. The number of cells analyzed in experiments performed in 96-well plates with different concentrations of various drugs is at least 500 cells per drug concentration. The number of cells in the CHX pulse and release live cell imaging experiments is at least 300 per experiment. The number of cells analyzed for the data shown in Figures 5 and 6 is mentioned in the respective figure legends. The number of cells analyzed for SNAP pulse/chase experiments is at least 200 cells per condition.

ETHICS STATEMENT

All experiments involving hESC were approved by the Canton of Vaud Ethics committee on human research (https://www.cer-vd.ch).